2017

In-Situ Measurement of Contact Area and Deformation of Soft Materials: Probing Adhesion Hysteresis

Michael Sedaille
Lehigh University

In-Situ Measurement of Contact Area and Deformation of Soft Materials:

Probing Adhesion Hysteresis

By

Michael D Sedaille

A Thesis

Presented to the Graduate and Research Committee

Of Lehigh University

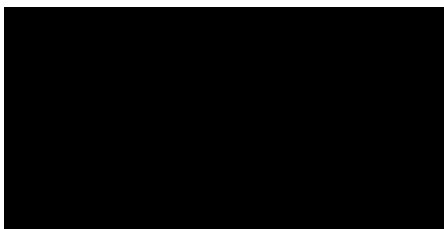In Candidacy for the Degree of

Master of Science

In

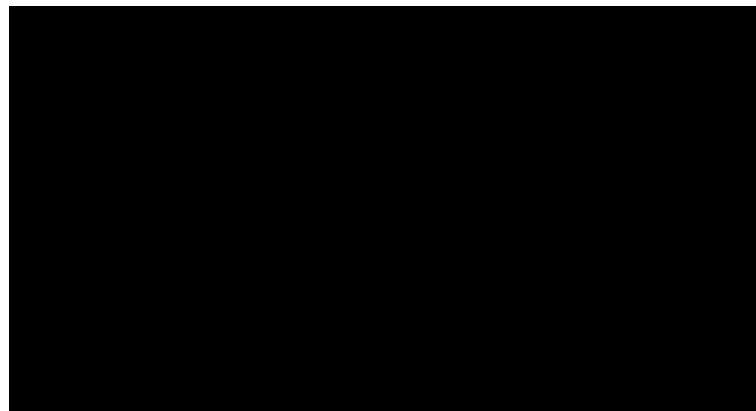Mechanical Engineering

Lehigh University

August 2017

This thesis is accepted and approved in partial fulfillment of the requirements for the Master of Science.

_____

Date

Acknowledgements

Table of Contents

Table of Figures

Table of Tables

Abstract

In this paper, we zoom in on the points of contact between the two materials in order to truly understand the surface-to-surface interface. We choose aluminum oxide (Ruby/Sapphire) spheres and polydimethylsiloxane (PDMS) discs to investigate the variability of real adhesive contact. An in-situ optical tribometer is built and implemented for use in obtaining forces of adhesion between PDMS and Ruby and comparing against the Johnson-Kendall-Roberts (JKR) contact model. Adhesion hysteresis is explored and compared to results found in the literature. High resolution in-situ imagery is coupled with custom data acquisition software to examine the relationship of contact area to applied force, loading rate, dwell time, and unloading rate. Contact area and pull-off force are shown to be dependent on applied force, dwell time, and unloading rate, while loading rate shows no major effect. Newton Rings in captured in-situ contact images are used to create three-dimensional models and height maps of the tensile region. This method provides accurate representations of surface and bulk behavior in a variety of contact conditions. A tensile zone is found at the edge of contact for all testing scenarios.

A. <u>Introduction</u>

Tribology has been important to the engineering of practically everything since the dawn of civilization and continues to dominate discussions about efficiency in modern mechanical systems. Overcoming the force of friction was just as important those dragging stones into place for the pyramids in Egypt as it is to lubrication engineers today. In Egypt, wooden sliding sledges piled with stone were dragged across wetted wooden planks to create the Statue of Tehuti-Hetep in 1880 B.C., and in 16th century China, sledge pullers took advantage of icy roads instead of wooden planks in order to transport stone to the construction of the Forbidden City[1]. These ancient builders may not have known the science behind their useful pulling techniques, but their makeshift engineering has grown into an essential field of science.

Today, we apply lubrications for basically all moving parts, whether they are solid lubricants or liquid ones. The application, effectiveness, and improvement of these lubricants, as well as their elimination in favor of low friction parts, is the result of Materials Tribology. It is common knowledge that friction wears down materials and can cause problems in mechanical systems, yet this awareness is just a taste of the field of contact mechanics.

Apart from Tribological applications, understanding contact mechanics is vitally important to science in general, industry, and everyday life. Learning the mechanics of soft matter is subsumed within a desire for understanding soft matter in general. In such a case, we provide opportunities to create materials with improved characteristics while also reducing our reliance on harvesting natural polymers.

Thanks to polymer research, the Rubber Manufacturers Association estimates that approximates 70% of all rubber used in manufacturing now is synthetic. Synthetic soft matter is particularly important for its application to bioengineering and medicine[2][3]. For example, soft polymers can resemble natural materials and are often used in their place. Biomedical objects like plastic implants and tissue scaffolds have been used for years to improve people's lives[4], and now they're being 3d printed to provide quick, custom parts to surgeons[5].

In this paper, we consider the contact mechanics of soft matter, particularly adhesion. Contact behavior of soft polymers and contact mechanics in general have been widely studied because of applications in numerous engineering fields. In industry, we see these polymers used in products like tires, brakes, paints, lubricants, foams, films and more. In these cases, the contact between the material and another substrate is especially important to its function. In nature and biology, contact mechanics plays a part on a microscopic scale, particularly with soft matter. The movement of small particles, organisms, and cells is often dominated by adhesion forces[6][7].

A.1 **Adhesion**

This study looks at adhesion that occurs because of van der Waals forces present between two materials. This dispersive adhesion is often observed macroscopically in liquids, where intimate contact between the liquid and a surface can be produced[8]. For example, rain droplets will follow along a wall and continue under a ledge, sticking to the underside of a window or gutter due to adhesive forces between the water molecules and the surface. This same principle of adhesion is present in all surface interactions, including those between two hard materials. The reason we don't see every days items adhering to each other like water on a window is because, with solids, the real contact area between surfaces is a small fraction of the apparent contact area[9]. In order to witness strong adhesions, the surfaces must be in intimate contact. The adhesive force is significant, but its effective range is short, and solids often have rough surfaces that prevent intimate contact[10]. In other words, the adhesive force is opposed by the elastic restoring force of the deforming materials[11]. When the elastic force is high, as it is with solids, the adhesive force is less noticeable.

Solid surfaces have an associated roughness that can prevent the intimate contact needed for noticeable adhesion. The tips of asperities present on two surfaces are the first areas to come into contact. If the materials have a high modulus (i.e. very stiff), then the asperities experience minimal deformation upon loading, preventing the rest of the surface from reaching a sufficiently close distance to form contact. In lower modulus materials however, asperities can be deformed more easily. As such, the surfaces of two materials can more easily form intimate contact as asperities deform to a height that permits adhesive attraction.

The large deformation available to soft materials is what makes them useful for gripping. Of course, there is more involved, but the increased area of real contact is central to this capability as large areas of adhesive contact are needed for gripping. Geckos make use of this phenomenon to walk along vertical and upside down surfaces. The contact area between their feet and these surfaces is made incredibly large by the bristle-like Seta lining their toes, adhering the gecko to smooth and rough surfaces alike[12]. The adherence is so strong that it can both counteract the force of gravity perpendicular to the adhesive force if the gecko is upside down. Such intimate contact is possible with clean, smooth, soft matter. Functionally, intimate contact is required in seals, O-rings, and other places where the proper adherence of a material to its enclosure is necessary to prevent leaks or separation.

There is also a desire to understand what happens to surface interactions as the mass of interacting objects shrinks in order to keep up with the miniaturization of modern technology. Though it is always present, adhesion effects are more substantial as the surface area to volume ratio of components gets larger. This leads to more microscopic tribological interactions that can cause unforeseen effects[13]. To mitigate unexpected failures, it is necessary to confirm the predictions of contact models with experimentation.

The forces responsible for adhesion play a huge part in surface characterizations, lithography, and various other applications of Atomic Force Microscopy (AFM)[14][15][16]. This technique uses a very small probe, with a tip radius on the order of nanometers, to scan a surface for topographical data. The cantilevered tip is dragged along, tapped across, or floated above the surface to collect

information on its height. In tapping and non-contact modes, the cantilever oscillates at a known frequency and with a known height. Van der Waals forces pull on the probe as it nears the surface, affecting the amplitude and frequency of oscillation and providing information about topography. In this case, a better understanding of adhesive forces leads to better AFM techniques and more accurate data.

A.2 Standard Models of Contact

The following contact models are early, simple models that are often still used in contact research today, including as a baseline for comparison with new methods of data acquisition or theoretical calculations.

A.2.a Hertz

Modern theories of contact mechanics are rooted in *Ueber die Beruehrung elastischer Koerper* (On Contact between Elastic Bodies) by Heinrich Hertz. This paper, published in 1882, outlined the first major understanding of contact area and has been built upon continuously to develop more accurate models[17][18]. Hertz defined a circular contact area of radius a_{Hertz} between a spherical indenter and sample.

$$a_{Hertz}^3 = \frac{PR}{K} \tag{1}$$

where P is the load, R is the equivalent radius, and K is the equivalent elastic modulus.

$$R = \frac{R_1 R_2}{(R_1 + R_2)} \tag{2}$$

6

where R_1 & R_2 are the radii of the spheres. Given the contact is between a sphere and a flat surface, we treat the flat surface radius to be ∞ and so R is equal to the radius of the single sphere.

$$K = \frac{4}{3}\left(\frac{1 - v_1^2}{E_1} + \frac{1 - v_2^2}{E_2}\right)^{-1} \tag{3}$$

where E_1 & E_2 is the elastic modulus for the indenter and sample and v_1 & v_2 is Poisson's ratio for the indenter and sample.

Distant points within each sphere will travel towards each other upon loading. The change in the distance between them is defined as δ.

$$\delta^3 = \frac{9}{16}\pi^2(k_1 + k_2)^2\frac{R_1 + R_2}{R_1 R_2}P_0^2 \tag{4}$$

Hertz verified this theory by viewing the contact of glass spheres with an optical microscope. Hertzian Contact mechanics, as it is now called, is succeeded by models that found errors with its calculations. For example, at low or zero loads, the predicted contact area is much smaller than the observed contact area. This is due, in part, to adhesive forces present in the interaction.

A.2.b **JKR**

In their paper *Surface Energy and the Contact of Elastic Solids,* Johnson, Kendall, and Roberts(JKR) explore the role of surface energy in contact area[17].

They reference earlier studies, including some of their own, that find the contact area

of loaded spheres does not match that of the calculated contact area proposed by

Hertz[19]. Their work adds the adhesive force, based on surface energy, into the

contact area equation. This addition makes sense of the inconsistencies within the

Hertz Model.

Every surface has an associated surface energy. This surface energy is a

product of the forces present in the creation of the surface. Separation of two bodies

requires work to overcome the adhesive forces present between the bodies. The energy

required to create the new surface is the free surface energy(γ) and is defined as:

$$\gamma = \frac{U_s}{\pi a_0^2} \tag{5}$$

where U_s is the surface energy lost in separation and the denominator represents the

area of contact before separation. Then, the work of adhesion $\Delta\gamma$, is defined:

$$\Delta\gamma = \gamma_1 + \gamma_2 - \gamma_{12} \tag{6}$$

where γ_1 and γ_2 are the free surface energies for each body and γ_{12} is the interfacial

free energy. This new term is used in defining the contact area. The radius of a

circular contact area is defined:

$$a_{JKR}^3 = \frac{R}{K}\left(P + 3\pi\Delta\gamma R + [6\pi\Delta\gamma RP + (3\pi\Delta\gamma R)^2]^{\frac{1}{2}}\right) \tag{7}$$

where P is the load, R is the equivalent radius, and K is the equivalent elastic modulus.

$$R = \frac{R_1 R_2}{(R_1 + R_2)} \tag{8}$$

$$K = \frac{4}{3}\left(\frac{1 - v_1^2}{E_1} + \frac{1 - v_2^2}{E_2}\right)^{-1} \tag{9}$$

8

Notice that given $\Delta\gamma = 0$, the JKR model reverts to the Hertz model.

The load/pull-off force at $a_{JKR} = 0$ is:

$$P_{a_0(JKR)} = -\frac{3}{2}\pi\Delta\gamma R \tag{10}$$

It is important to notice, as pointed out within the work, that the pull-off force is independent of elastic modulus and so must be the adhesive force. It is also noted that the radius of contact at zero load is nonzero, as seen in experimentation:

$$a_{JKR}^3 = \left(\frac{6\pi\Delta R^2}{K}\right)^{\frac{1}{3}} \tag{11}$$

A.2.c **DMT**

At around the same time as JKR, another trio of scientists developed a theory of contact that takes into account the attractive forces present in non-contact regions[20]. Derjaguin, Muller, and Toporov(DMT) penned a paper partially in reply to JKR alleging a different approach was necessary. In reference to JKR, Dahneke[21], and work done by Bradley on cohesion of smoke particles[22], DMT stated that the current work, particularly Dahneke's work, ignored the effects of deformation and many other things and thus was "grossly erroneous". After considering these other influences, DMT gives contact radius(a) as

$$a_{DMT}^3 = \frac{R}{K}(P + 2\pi\Delta\gamma R) \tag{12}$$

where P is the load, R is the equivalent radius, and K is the equivalent elastic modulus.

$$R = \frac{R_1 R_2}{(R_1 + R_2)} \tag{13}$$

$$K = \frac{4}{3} \left(\frac{1 - v_1^2}{E_1} + \frac{1 - v_2^2}{E_2} \right)^{-1} \tag{14}$$

The load/pull-off force at $a_{DMT} = 0$ is

$$P_{a_0 (DMT)} = -2\pi \Delta \gamma R \tag{15}$$

Here, we notice that the pull-off forces for JKR and DMT theories are similar, but not the same. Both models seem to be verified through experimentation, though under different circumstances.

A.2.d **MYD & Others**

A connection between the JKR and DMT models was created in 1977 by Tabor, who concluded the adhesion was depended on surface forces, surface roughness, and the ductility of the solids[23]. He clarified discrepancies between the two models and suggested shortcomings in both cases that could be accounted for with a new parameter. Using this new Tabor parameter, Tabor generalized the current theories of contact. The Tabor Parameter(μ) is defined as

$$\mu = \left(\frac{R(\Delta \gamma)^2}{\left(\frac{3}{4} K \right)^2 z_0^3} \right)^{\frac{1}{3}} \tag{16}$$

where R is the equivalent radius, γ is the free surface energy, K is the equivalent elastic modulus, and z_0 is the equilibrium spacing according to Lennard-Jones potential.

Muller, Yushchenko, Derjaguin (MYD) followed up this new theory with the result that there is a smooth transition between the JKR and DMT theories in accordance with the Tabor parameter[24]. Maugis further clarified the transition between the two models using the Sneddon approach for contact[25][26].

More comprehensive models of contact have been developed[27][28][29][30], however, adoption of these models can require significantly more calculation than the simplified models presented by DMT and JKR[31]. These old models are often accurate enough to be used as long as their limitations are taken into account, and have been used as recently as 2017[32][33]. In our case, JKR is most applicable because it remains accurate. However, it is useful to know Hertzian mechanics, as well as DMT and MYD techniques, to truly understand how the JKR approximation fits into the grand scheme of adhesive contact.

Table 1: Comparison of Contact Models

Model	Applications	Assumptions
Hertz	Stiff solids Any radius	Neglects adhesion Single point contact at zero load
JKR	Low modulus solids Large radius	Tensile and compressive stress within contact area Adhesion from surface energy in contact zone only Neglects adhesive forces outside of contact area
DMT	High modulus solids Small radius	Hertzian contact model within contact zone Adhesive forces occur outside contact zone
MYD	Solids with modulus outside of JKR or DMT Any Radius	Makes use of Tabor parameter, Lennard-Jones potential, Dugdale adhesion/stress

A.3 **Modern Related Research**

Standard contact models provide an excellent basis for investigating contact behavior of elastic materials, but no material is perfectly elastic. Viscoelasticity is present in all materials, significantly complicating measurements taken to relate contact area, deformation, and force. This can be mediated to some extent, but in nearly all cases viscoelasticity will play a part and must be accounted for. Along with viscoelasticity is a host of other complications in this type of investigation that are present in the literature.

A thorough review of fracture and adhesion of soft materials is outlined in Creton *et al*[34]. This is a very useful resource for understanding historic advances in soft matter surface interactions. Such an in-depth assessment will not be found in this paper, but we have attempted to include particularly pertinent research. This research is based on the foundation built by Krick *et al* 2012 [35]. Similar instruments have been built for imaging of tribological and adhesive testing[11][36][37][38][39], however the instrumentation used below has especially exceptional resolution in imaging and in data capture frequency for similar sized studies.

The role of surface roughness has been studied by Lorenz *et al* 2013[40] whereby adhesive pull-off force was determined to decrease with randomly rough surfaces as opposed to smooth ones, caused mainly by reduction in real contact area. More in depth analysis on surface roughness has been performed by Persson[10][41][42]. These analyses have shown a dependence of adhesive force on viscoelastic energy dissipation at the crack tip in conjunction with contact area, as well as a generally decreasing work of adhesion after run-in, the period where free oligomers transfer freely from the soft material to the previously clean indenter surface. Work of adhesion is made independent from number of indents through extraction of free chains from the surface. Non-adiabatic viscoelastic energy dissipation at the crack tip results in an adhesive force that is larger upon pull-off then upon approach. This is referred to as adhesion hysteresis[43]. In crack propagation, the viscoelastic energy dissipation results in strongly increasing the energy necessary to propagate a crack[44].

The extraction of free chains from the surface is one of many treatments done to isolate components of adhesive force. Surface interactions have a significant effect on overall adhesion of soft materials like PDMS. Chaudhury & Whitesides 1991[11] and Chaudhury & Whitesides 1992[45] showed significantly increased adhesion after surface oxidation, and surface functionalization allowed for separation of surface effects from bulk viscoelastic effects. Silberzan 1994[46] shows hysteresis loops as a result of hydrogen bonding across the interface between Si-OH molecule. Experimentation in with HCl surface modification supports this theory, as it showed increased adhesion.

Separately, Jagota 2002[52] explores natures applications of adhesive interfaces through fibrillary microstructures present in many organisms. Fibrillar structures allow room for deformation of fibrils, so that the carpet of fibers may act as a plastic material for greater contact area and thus greater adhesion in presence of roughness. The advantage of fibrils over a solid soft material in contact is the ability to use stiffer materials for fibrils so that there is no undesired stickiness at the interface, relying on Van Der Waals forces exclusively for adhesion.

Adhesion as a function of separation rate is explored in Ruths 1998[47], showing a positive correlation with most materials. Further investigation by Kovalchick 2013[48] confirms this dependence in peel tests. Vorvolakos 2003[49] investigates the relationship of loading force with contact area and sliding velocity of PDMS elastomers. Results showed heavy dependence on molecular weight due to the subsequent contact area and highlighted the intricacy of the adhesive interface. Similar research in shear induced adhesive failure was described in Chaudhury 2007[50].

Applicable mechanics of interfacial rate processes are outlines in Ghatak 2000[51]. For an elastic ball on a flat, the growing and shrinking contact at the surface follows a work of adhesion (W) nearly equal to strain energy release rate (G)

$$G = \frac{\left(\frac{4E^*a^3}{3R} - P\right)^2}{8\pi E^*a^3} \tag{17}$$

that is function of contact radius a, ball radius R, pressure P, and equivalent elastic modulus E^* where

$$E^* = \frac{1}{\left(\frac{1 - v_1^2}{E_1}\right) + \left(\frac{1 - v_2^2}{E_2}\right)} \tag{18}$$

However, viscoelastic energy dissipation results in thermodynamic irreversibility in contact mechanics studies such that $W \neq G$ and in fact

$$G - W = W\phi(a_T V) \tag{19}$$

where ϕ is a dimensionless viscoelastic dissipation function that depends on a_T(the WLF shift factor), the viscoelastic properties of the materials, crack speed V, and temperature T.

In general, three phenomena dominate adhesive indenting interactions: bulk strain energy release dependent on material properties, local viscoelastic strain at the crack tip, and intermolecular forces. Intermolecular forces, namely hydrogen bonds and dispersive adhesion, effect the total force of adhesion differently. As demonstrated by Ghatak 2000[51], dispersive adhesive contact with no hydrogen bonding shows almost no rate dependence, while the opposite is true for hydrogen bonded contact. This suggests a connection between bulk/local viscoelastic strain and hydrogen bonding at the surface. The connection is relaxation time. The bond number

dependence of relaxation time explains the requirement for hydrogen bonding at the surface to see rate dependent adhesive forces. These bonds couple bulk and surface viscoelastic phenomena with intermolecular forces. Because of this, we know equation 19 is a generalized case because it has no dependence on bond number. We can expect to see a rate dependence of adhesion force in experimentation because viscoelastic properties act to dissipate energy otherwise going to break bonds/polymer chains at the interface.

B. __Methods__

B.1 **Tribometers**

Tribometers come in myriad shapes and sizes because they are built with their samples in mind. Most often this includes sliding a material sample against a substrate that represents a typical contacting material. Friction force, wear, and normal force are all recorded over time or 'cycles' of testing. This data will show the points where a material wears due to friction, how the wear affects the mechanics of the material, and what is happening at the surface to surface interaction. This data helps estimate a useful lifetime for the sample.

B.2 **In-Situ Imaging**

In-situ imaging is hardly a new technique. Such a method provides valuable information about what led to the final results of a research subject. It is easy to see the aftermath of a wear test and conclude that friction has led to the degradation of a material, but in-situ investigation shines a light on the causes and mechanisms of the wear, a peek at the evolution of a wear scar. This is not only applicable to tribology, however.

In-situ magnetic resonance imaging has been used to produce 3D models of neuronal pathways in a rat brain[53]. The growth of carbon nano-fibers has been viewed in-situ using a transmission electron microscope, allowing researchers to see what happens at the gas-solid interaction of nickel and methane [54]. In-Situ Raman spectroscopy measurements have been used to monitor doping of graphene

transistors[55]. In-situ studies are important tools to many areas of science, including materials tribology.

In-situ tribometers have been used in the study of solid lubricants in a manner that is very similar to the techniques we apply in our studies [36], [37]. In *Chromik et al.,* transfer films and interfacial dynamics were observed through a sapphire hemisphere. The in-situ observations motivated the establishment of four velocity accommodation modes (VAMS) that better described tribological performance of solid lubricants used in aerospace applications. An even more related study was done by *Wahl et al*[37]. quantifying transfer film thicknesses through optical observation. A Newton Rings method was used to quantify the evolution of the transfer film in real time. We will use this Newton Rings technique to quantify real contact area using the Lehigh in-situ optical tribometer.

B.3 Lehigh In-situ Optical Tribometer (LISOT)

Lehigh's in-situ optical tribometer is a purpose-built instrument that is designed to allow for non-intrusive imaging of sliding or contacting surfaces during experimentation.

B.3.a LISOT: Design

The LISOT has 3 main systems that sit within the aluminum base structure, the xy-stage, the z-stage, and the imaging system. It sits on a Minus k Technology isolation stage, which rests on a 1,000lb granite isolation table for vibration damping.

This is all caged off by a quasi-cleanroom structure made of plastic sheeting to prevent dust and other contaminants from tampering with tests.

The foundation of the xy-stage system consists of two manual linear micrometer positioning stages. The y-stage is placed perpendicular and atop the x-stage. Above these stages is a PI M-683.2U4 piezo motorized precision stage in the x position, followed by a PI P-628.1CD piezo linear stage that holds the sample holder. This setup allows the possibility to accommodate for multiple different test cycles on one substrate by changing the positioning. The aluminum sample holder extends in the x direction to float above the imaging system and below the z-stage system and is capable of holding 1 inch glass discs as well as standard 3-inch microscope slides. FEA was performed in SolidWorks to confirm that negligible deflection was present in the sample holder due to indentation loads.

The imaging system consists of perpendicularly aligned optical components. The xy plane consists of the CCD camera and LED light whose optical paths are reflected in the positive z direction by a beam splitter and mirror where they culminate at a microscope objective. This allows for viewing of object in the sample holder from below. The optical components are placed on an adjustable z-stage for focusing the objective lens without changing the distance of the optical path.

The lens used is a 10X Olympus Plan N objective. The coaxial lighting is an XPE2 Amber 590nm wavelength LED driven by an A011-D-V-350 350mA driver purchased from Digi-Key. This powered by an Acopian W20FT370 power supply. The LED color is based on the successful in-situ LED lighting of the optical tribometer used by Krick *et al.*[35]. The camera is a Ximea xiD MD120xU-SY 12-

megapixel scientific grade camera with a pixel size of 3.1 μm. Paired with our 10X objective, the camera takes images with a pixel size of 0.31 μm. The rest of the optical system was manufactured my Marcel Aubert for use by the University of Florida and has now been adapted to the LISOT system.

The z-stage system is the most technically complicated part of the tribometer. Attached to a vertical aluminum support is a manual linear micrometer positioning stage and PI P-628.1CD piezo linear stage providing programmable travel in the $\pm z$ direction. The z-piezo is supporting an aluminum structure that reaches out above the sample holder. This structure holds the cantilever-mounted ruby probe and two micrometer-mounted capacitance probes.
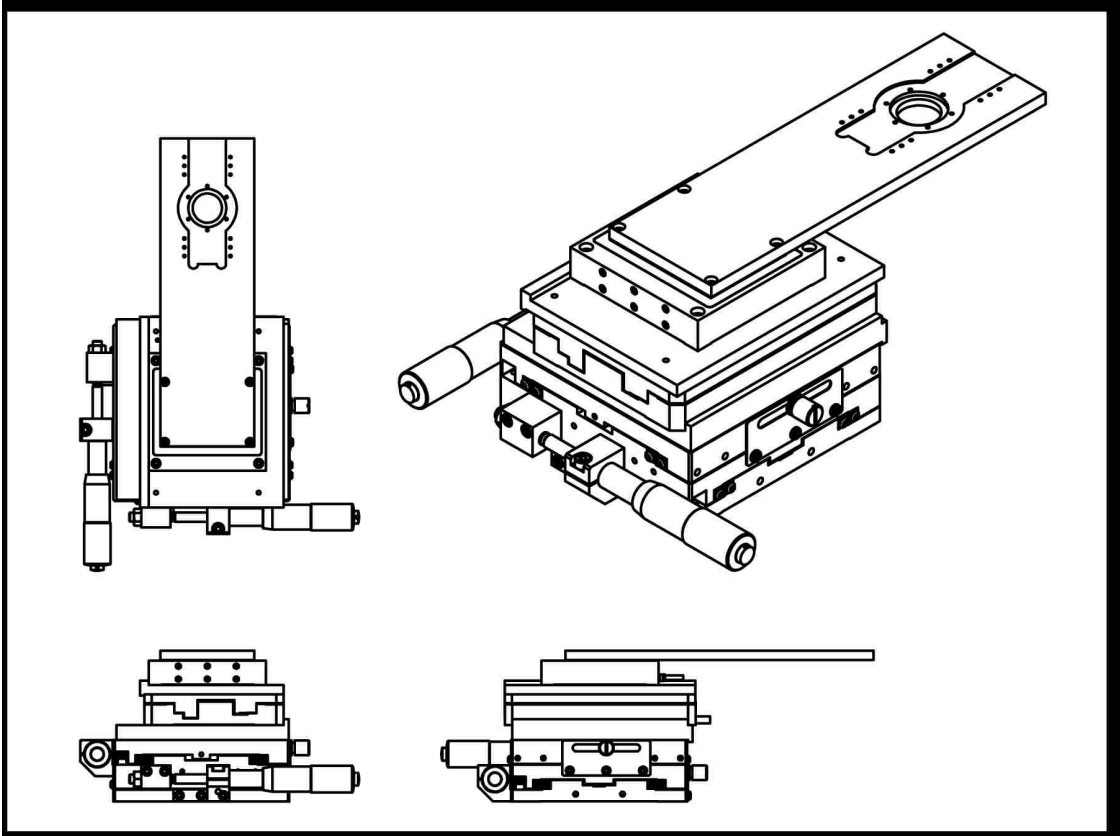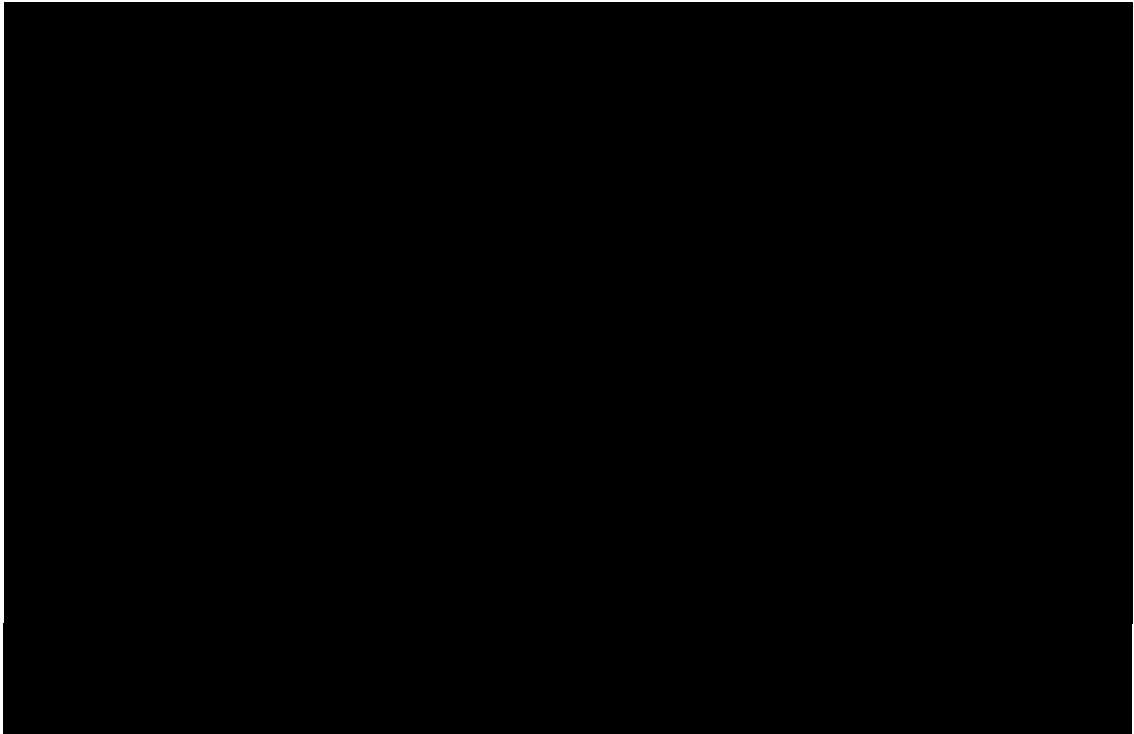
The ruby spheres are glued to set screws that allow them to be secured in the flexible cantilever. The cantilever consists of two waterjet cut titanium sheets that allow for rectilinear flexure. When the z-piezo is lowered, so is the attached cantilever. When the ruby probe makes contact with a substrate, the cantilever will flex. The z-stage provides position information, but does not provide the capability to apply a specified force. With the cantilever, however, Hooke's Law allows us to gather and specify forces on the ruby probe.

$$\text{Hooke's Law:} \quad F = kx \qquad\qquad (20)$$

where F is the force on the probe, k is the stiffness of the cantilever, and x is the flex of cantilever obtained by the capacitance probe. Cantilever stiffness is recorded before

testing. Known masses are used to create deflection in the cantilever. This deflection is measured, recorded, and plotted against gravitational force to find k. For our cantilever, normal stiffness k is $510 \frac{\mu N}{\mu m}$. The lateral stiffness is ignored because there is no lateral movement in the LISOT setup.

The micrometer-mounted capacitance probes are used to measure the displacement with respect to the position of the z-piezo. The capacitance probes are from Lion Precision and are driven by a Lion CPL290 Driver. These probes can measure sub-nanometer resolution in the distance between themselves and the cantilever. Changes in this distance correlate to a change of capacitance between the probe and cantilever, which is detected by the driver. The driver produces an output voltage proportional to the distance which can be converted with the known $\frac{\mu m}{V}$ parameter.

All electronic components of the LISOT are controlled through LabVIEW and a National Instruments BNC-2120 DAQ Device. All output signals providing data also return through this setup to provide instantaneous analysis in LabVIEW.

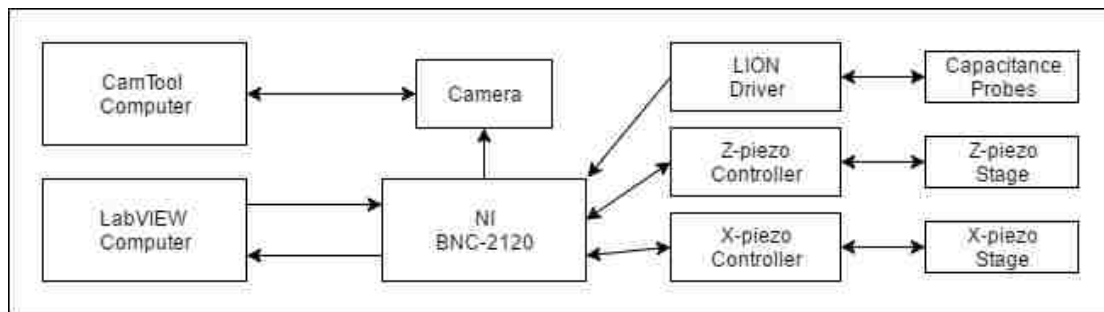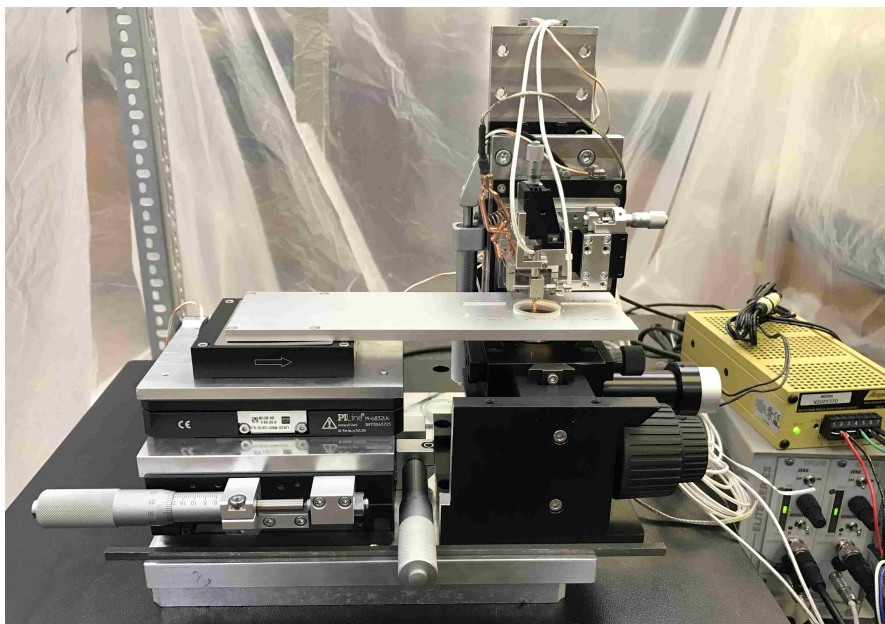**Figure 4: LISOT Communication Schematic**

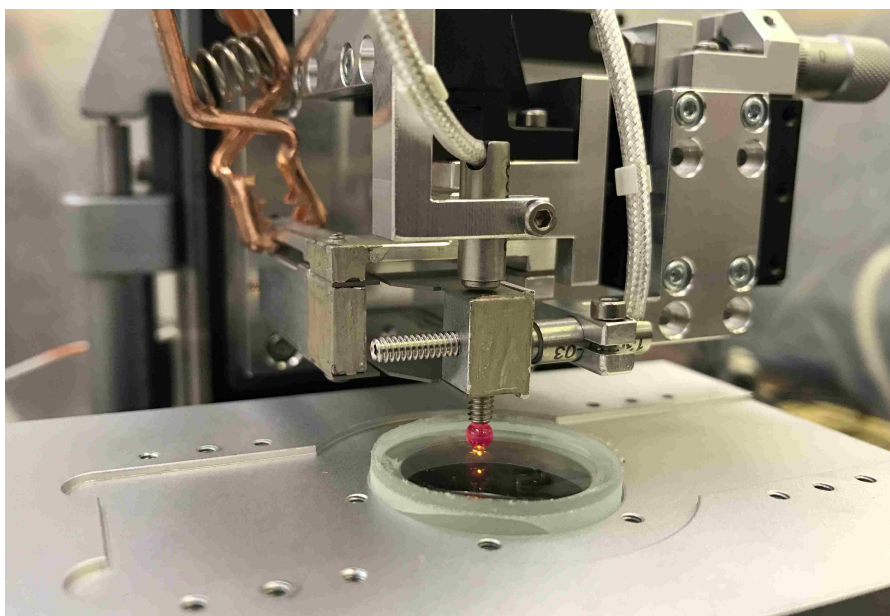**Figure 5: Lehigh's In-Situ Optical Tribometer**

Figure 6: LISOT Cantilever Close-up

Ruby probe in contact with PDMS, under-lit by coaxial lighting through objective lens. Micrometer positioned capacitance probes measure the change in the distance to the cantilever block. Sample holder maintains positioning of glass window and PDMS substrate.

B.3.b **LISOT: Indenting**

Indenting with the LISOT is controlled by a LabVIEW code designed specifically for tribometers. This code has been built upon and adjusted to fit the needs of Lehigh's tribometers, like the LISOT. The user inputs experimental conditions and the code organizes the output data from the tests into excel files.

Before true data can be extracted from a test, the indenter and substrate must be "run-in" to reach a steady state adhesion force[56][40]. Free oligomers present from un-crosslinked polymer chains act to change the mechanics of contact as they transfer to the surface of the ball. These oligomers can change the interfacial interaction energy of either surface as well as the required pull-off force. Once this process has reached an equilibrium, tests can be run without worrying about appreciable drift due to changing surface environments.

After run-in, the actual testing varied the indenting speed, hold time, and pull-off speed of the ruby sample to look for effects on contact area and adhesion force. The indenting speed is the speed at which the ruby met the PDMS substrate. Dwell time refers to the amount of time that the ruby ball and the PDMS remained in contact at a fixed load. Pull-off speed is the speed that the ruby ball came out of contact with the PDMS substrate. Trials were based on a 1, 10, 100 numbering system. Each indent would vary the indenting speed between $1\frac{\mu m}{s}$, $10\frac{\mu m}{s}$, and $100\frac{\mu m}{s}$, vary the dwell time between 1,10, and 100 seconds, and vary the pull-off speed between $1\frac{\mu m}{s}$, $10\frac{\mu m}{s}$, and $100\frac{\mu m}{s}$. This is a total of 27 different indenting scenarios. Each test included the 27

indenting scenarios at a constant load. The load was changed between tests at 0mN, 1mN, 10mN, and 100mN. Tests were performed in air and water.

In all tests, the ruby began in a position where it was significantly out of contact. It was then driven by the z-piezo towards the PDMS at the defined rate. As the ruby ball approaches the PDMS surface, the adhesive forces begin to pull the two surfaces towards each other. The static PDMS pulls the flexible cantilever down into contact, providing a momentary negative force on the ruby ball. At this point the adhesive force is equal to that of the elastic restoring force of the cantilever. As the z-piezo continues to move down, the negative force increases to zero, at which point adhesion keeps the surfaces in contact even with zero load. In the case of 0mN tests, the probe would then unload. In the case of 1mN, 10mN, and 100mN tests, the probe would continue to indent to the specified load before pulling off.

Table 2: Example LISOT Data from the First 0.1 Seconds of an Indent Cycle

Date:	6/14/17		User Name:	Sedaille						
Project:	Ruby PDMS		Substrate Sample:	PDMS						
Pin Material:	Ruby Pin		Substrate Descripti	xx						
Pin Radius:	1.5 mm		K normal:	510.009	uN/um					
Environment:	Air		K lateral:	7697.54	uN/um					
Cycle:	1									
time(seconds)	Fn (uN)	stdev (Fn)	Ff (uN)	stdev (Ff)	mu	stdev (mu)	x-stage (um)	z-stage (um)	Camera Trigger (V)	
0.003	55.513	18.641	152.932	80.961	3.093	2.059	-0.049	-0.038	4.824	
0.007	-58.483	22.711	32.199	98.765	0.03	2.305	-0.014	-0.027	5.003	
0.012	1.216	43.496	79.103	104.525	-1.878	14.353	0.027	-0.03	5.004	
0.017	34.654	34.999	126.564	101.282	1.092	23.49	-0.012	-0.003	4.993	
0.022	-66.652	16.106	24.618	126.603	-0.627	2.377	0.008	-0.01	5.009	
0.027	33.186	35.015	132.892	126.199	-1.606	43.5	0.011	-0.014	5.014	
0.032	-0.566	42.953	148.713	105.113	-1.492	18.949	-0.039	-0.009	5.003	
0.037	-57.448	24.441	145.009	85.618	-3.633	4.488	0.067	-0.013	4.982	
0.042	39.056	12.998	99.669	137.967	4.384	8.708	0.036	0.009	5	
0.047	-34.109	30.715	136.057	136.855	-3.689	5.321	0.017	-0.02	5.02	
0.052	-13.773	35.404	117.072	108.95	-1.517	8.833	-0.004	-0.011	4.997	
0.057	24.276	22.719	105.998	75.813	3.28	22.085	-0.006	-0.019	5.001	
0.062	-45.892	13.553	111.052	90.848	-2.946	2.766	0.009	-0.034	2.921	
0.067	19.664	19.938	41.133	129.134	0.291	12.671	-0.012	-0.019	-0.004	
0.072	-3.815	24.262	183.518	127.333	-17.597	41.801	0.011	-0.009	0.001	
0.077	-16.338	18.036	55.488	103.394	1.979	29.998	-0.01	-0.012	-0.004	
0.082	2.474	15.6	71.192	75.678	2.934	18.512	-0.012	0.028	-0.007	
0.087	-26.155	13.912	165.074	116.351	-10.544	46.372	-0.01	-0.018	-0.007	
0.092	30.251	11.149	45.88	124.509	4.481	11.274	0.019	-0.019	-0.004	
0.097	-39.245	27.925	185.1	92.304	-5.823	17.088	0.041	-0.015	-0.012	
0.102	-16.235	37.585	128.031	99.446	2.408	11.399	0.05	-0.016	-0.007	

Data from the LISOT is exported directly in excel format, providing force and z- piezo position as a function of time, from which cantilever displacement and indentation depth can be calculated. The excel data was loaded into a Matlab script that ripped the tests into the 27 cycles. It then found the adhesion force and errors in load, unload, and hold time for each cycle based on user specified points along the force-displacement curve.

$$Penetration\ Depth\ (\delta) = (z_0 - d) = \left(z_0 - \frac{F}{k}\right)$$

$$Pull - Off\ Force\ (F_{adh}) = kd$$

where z_0 is the position of the z-stage at zero load, d is the z-axis displacement of the cantilever, F is the load, k is the cantilever stiffness.
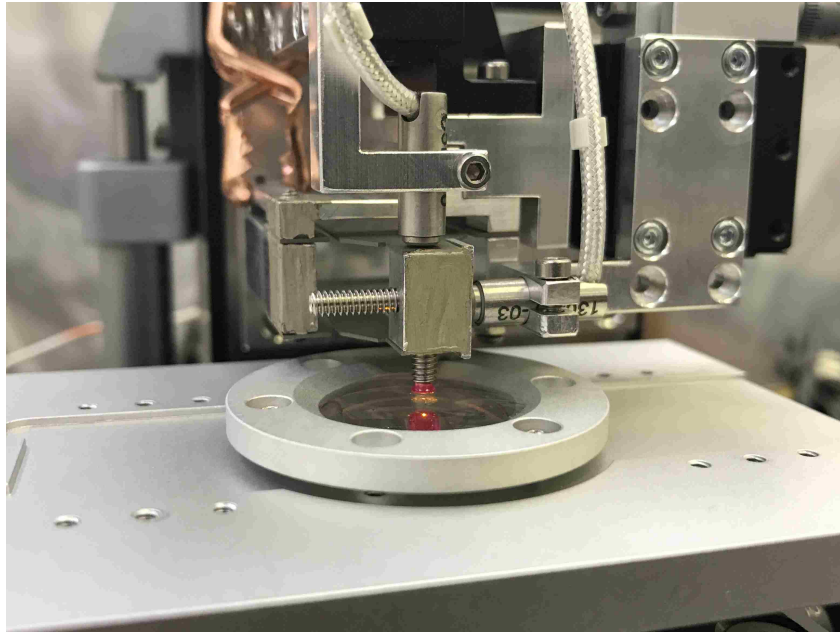

Figure 7: LISOT Indenting in Water Environment

A 3mm ruby probe indents a PDMS sample under water using a mount for liquid environments.

B.3.c **LISOT: Imaging**

Imaging for the camera is done both through a combination of LabVIEW triggering and Ximea CamTool. Ximea CamTool allows for adjustments to typical camera features like framerate, resolution, and exposure. It can display a live feed of the camera while recording and saving at a framerate of up to 16 fps. Frame captures are handled in two ways. If using exclusively Ximea CamTool, the camera can be commanded to capture images and save at a defined rate (i.e. frames per second) or at max speed, were the program will capture and save as many frames as the computer processing will allow.

A second way of image capture involves triggering the camera directly with a 5-Volt digital signal. The LabVIEW code can be set to generate a signal from the TI to trigger the camera at a specified rate, just as the LabVIEW data saving rate is specified. The triggered images are recorded and saved through Ximea Camtool, just as they would be when triggered from the program itself. Using LabVIEW for triggering gives us the flexibility of automatic image capture at different capture rates. For example, the LabVIEW code can take fewer pictures during slow contact speeds or when there is no contact in order to save storage space.

Images taken by LISOT show Newton Rings, concentric fringes of bright and dark interference. The very inner 'full' circle is the contact of the ruby sphere and PDMS. At locations of contact, light reflects off the top surface of PDMS and bottom surface of ruby, which are at the same optical location. At the ruby, however, a 180-degree phase shift is imparted on the light wave due to the changing index of refraction. This reflected light interferes destructively with the light reflected from the

PDMS surface and so the contact area is dark. Higher order interferences exist moving radially away from the 0th order destructive interference at the contact area. Bright fringes represent locations where the surface of the ruby sphere is a multiple of $\frac{\lambda}{2}$ away from the surface of PDMS, so light travels a total distance of λ more and interferes constructively. Dark fringes represent locations where the optical path from the surface of the ruby sphere to the surface of PDMS is $n\lambda \pm \frac{\lambda}{4}$ and so light travels a total distance of $\frac{\lambda}{2}$ more and interferes destructively.

Constructive interference at separation distance $d_c = n\frac{\lambda}{2}$

Destructive interference at separation distance $d_d = \left(\frac{2n+1}{4}\right)\lambda$
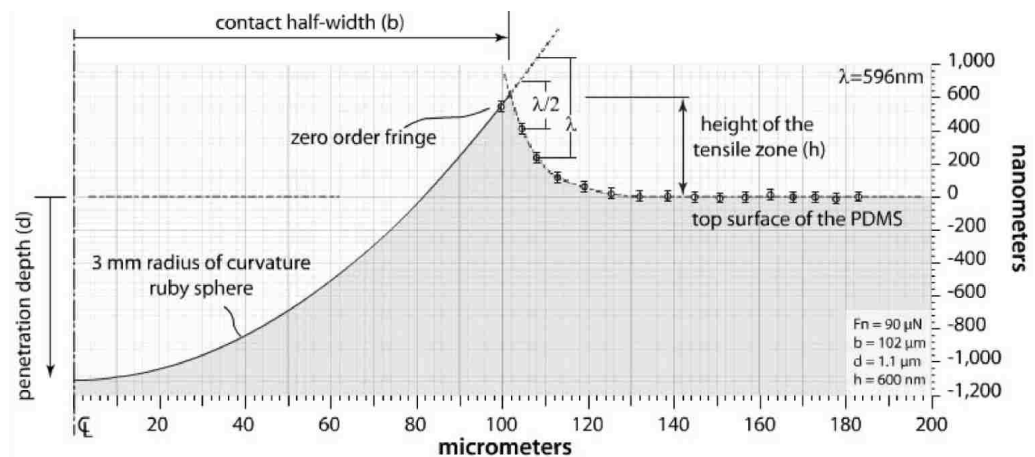

Figure 8: Interference Fringes Provide Valuable Data

Locations of constructive and destructive interference fringes correspond directly with changes in distance between the PDMS substrate and the ruby probe. By subtracting the known curvature of the probe from the distances given by interference fringes, it is possible to map the height of the tensile zone surrounding the contact region.
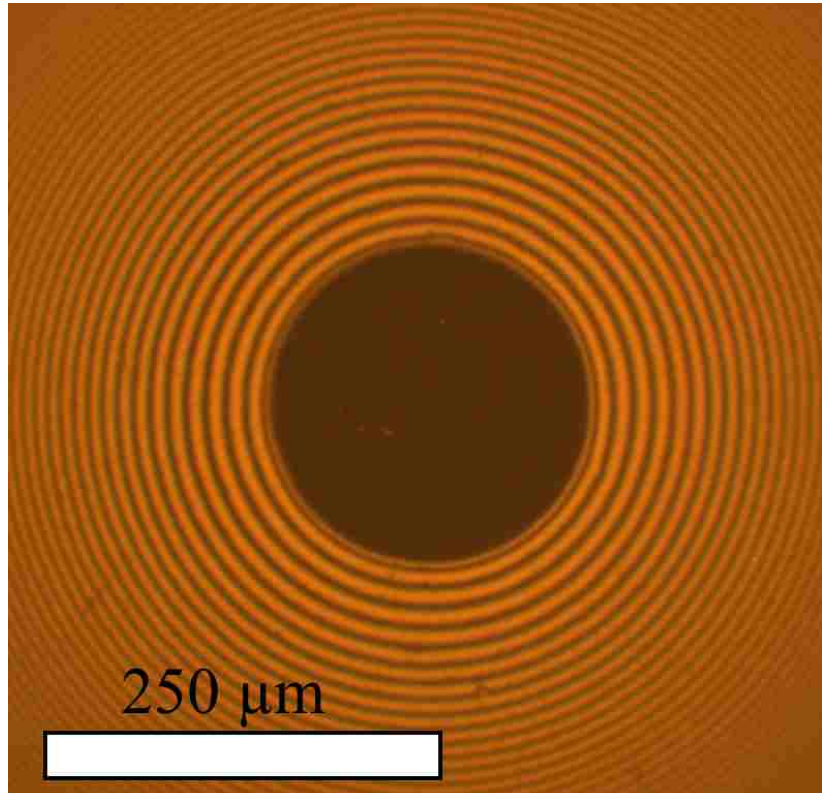
29

Figure 9: Newton rings captured by the LISOT imaging system

Photo results of the in-situ optics are shown. Coaxial illumination is produced by a 595 nm orange LED. This was taken directly after first contact where the load is about zero. Real contact is shown in the dark central circle which is . Rings are present due to interference at the interface. Concentric fringes present information about the distance between the surfaces. These images are 'unwrapped' by post processing for use in tensile zone height map construction.
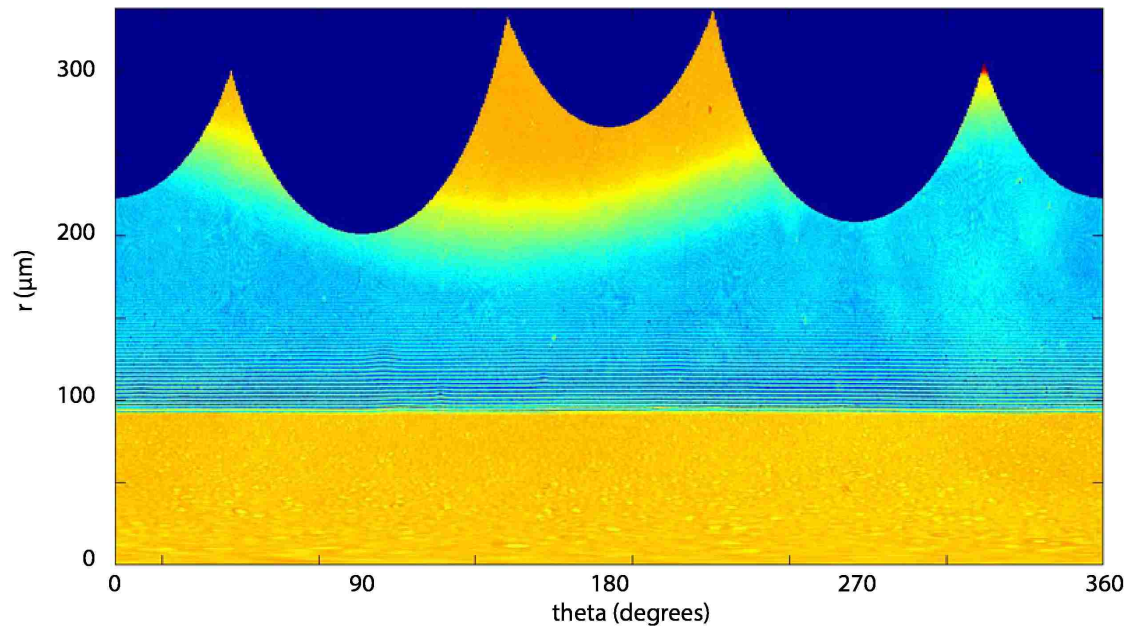
B.3.d **LISOT: Post Processing**

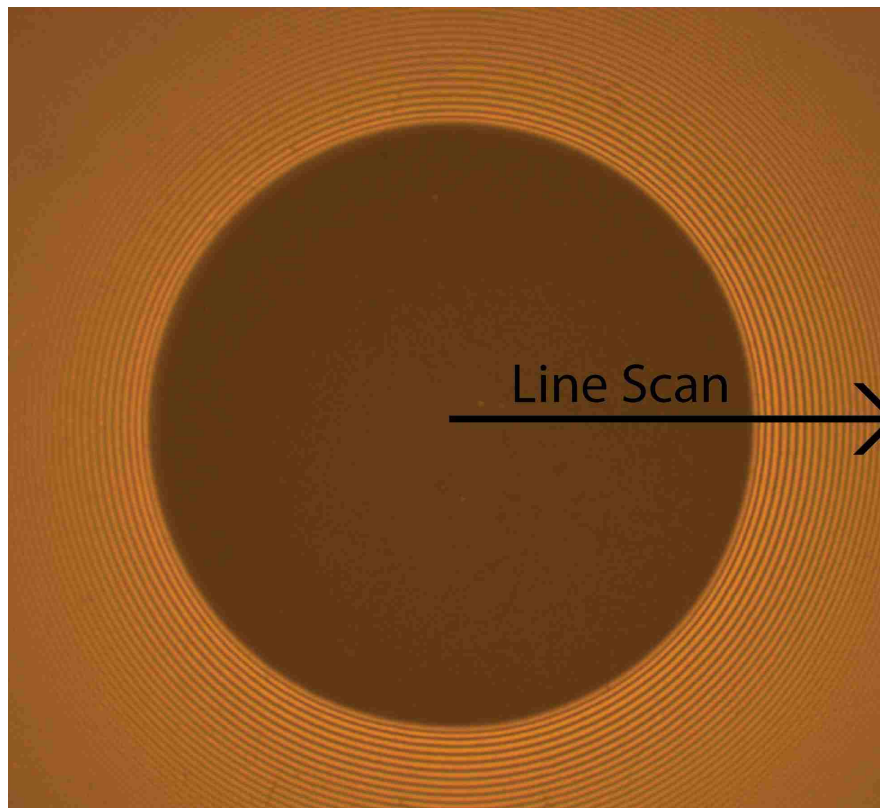**Figure 10: Newton rings unwrapped for processing**

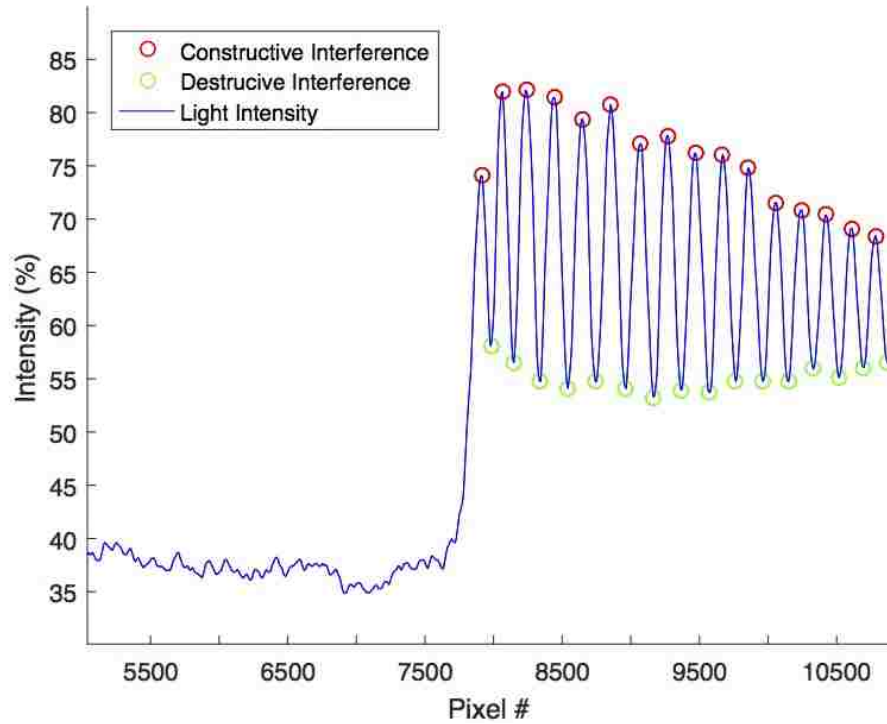**Figure 11: Direction of Peak/Valley Finding for Fringe Position Data**

Figure 12: Light Intensity Along Radius of Newton Rings

Considerable post processing was required to consistently collect data on contact area and tensile zone geometries as a function of time. Much of this was achieved through MATLab. Bitmaps were converted into matrices where a thresholding value was used to separate the large dark area of contact from light and dark interference fringes. Contact area was recorded based on the pixel size and number of pixels with values above the threshold. Fringe location were recorded as a function of degrees about the center of contact (Figures 11& 12). This was done using the unwrapped contact image (Figure 10). Three-dimensional positioning for points along the surface was possible using this technique. Height in the z direction was obtained based on the wavelength of the coaxial illumination, the number of fringes from dark contact area, and the radius of curvature of the ruby indenter. Two dimensional x,y or r,θ was obtained from pixel location in the image.

32

B.4 **PDMS**

Polydimethylsiloxane is a multipurpose polymer with ubiquitous presence in everyday life. This organosilicon is part of a group of compounds that makes up a huge part of the materials typically used for everything from sealants, lubricants, and cosmetics, to lithography and silly putty. Recently, PDMS is being used increasingly in electronic applications. Highly applicable mechanical and chemical properties lend to the versatility that PDMS is known for [57].

The mechanical and chemical/biochemical properties of PDMS are fairly well documented[58][59][60]. Elastic modulus is dependent on mixing ratios and curing time/temperature and is in the range of 1.32 to 2.97 MPa. Poisson's ratio of is 0.499 is a common accepted approximation used in literature for small strains. One of the most widely used PDMS elastomers is Sylgard 184 from Dow Corning. This is a two-part liquid that cures in 48 hours when combined, or quicker with heat treatment. Typical ratios of the base to curing agent are in the area of 10:1, however, this ratio can be adjusted to impart different mechanical properties. For example, the elastic modulus increases as the ratio increases up to 9:1, at which point the modulus begins to decrease[58].

PDMS also has fairly stable mechanical properties through a large range of temperatures (-100°C to 100°C) and timescales, including a high dielectric strength ($\approx$ $14\frac{V}{\mu m}$), making it a reliable material in microelectronics and microelectromechanical systems (MEMS)[61]. It is clear, chemically inert, and easy to handle, making it a friendly material for almost any application. Being biocompatible and non-toxic, it is

used in pacemakers, catheters, and other implants[62]. PDMS does not show appreciable absorption or reaction to the typical laboratory solvents isopropanol, methanol, and acetone, so it can be easily cleaned, sterilized, and/or sonicated.

The PDMS used in our experiments is Sylgard 184. Samples were prepared in a lab environment by combining 10 parts base liquid a to 1 part curing agent in a plastic cup for a total of over 20 grams of liquid. After mixing, the uncured PDMS was placed under vacuum for 30 minutes. This was done in a VWR Vacuum Oven model # 10752-398 at room temperature (20°C). The liquid was then carefully deposited on one-inch diameter Edmund Optics glass optical windows using disposable pipette tips. The glass discs provide a sturdy foundation for indenting, a clear window for viewing, and have a stiffness of 64 GPa so as to provide no added deformation. They are held in 25mm diameter cylindrical PTFE cavities that allow for a 25mm diameter, 2mm thick 'disk' of PDMS to be molded directly atop the glass. The PTFE mold holds 16 separated samples and it was placed in the Vacuum oven at 90°C for 2.5 hours. Both the free-air side and the glass side of the PDMS can be used for indenting after curing.

Using an AFM, the PDMS was tested to find the elastic modulus with the result of 1.87 MPa. Due to results presented in this paper, AFM measurements of soft materials with adhesive surfaces cannot always be considered completely accurate. The samples were also measured on a Scanning White Light Interferometer (SWLI) to validate the intended thickness range. Thicknesses of samples were between 1.8mm and 2.2mm.

B.5 Ruby/Sapphire

Ruby is a variety of corundum, the mineral also responsible for sapphire. These gems are $\alpha - $ alumina (Al_2O_3), a particularly stable form of alumina[63]. Ruby spheres are chosen for a few reasons. Ruby/Sapphire spheres provide a relatively smooth, hard, and stiff surface with which to form intimate contact. Hardness provides peace of mind that micro scratches and other wear will not develop, hindering accurate data collection. The modulus of elasticity varies form 345- 494 MPa, but the value used most is 350MPa. Stiffness on the order of 350MPa is high enough to ensure that most of the deformation is seen within the PDMS. The rubies are unlikely to cause chemical reactions with a substrate or the environment. They are also optically transparent, inexpensive, single crystals capable of a polish, as opposed to other materials that may use sintering or a binder to form a hard, smooth sphere.

Ruby spheres of 1.5mm and 3mm diameters were purchased from Swiss Jewel and used in testing. They were sonicated in acetone for 20 mins and methanol for 20 mins and glued to 5/8-inch-long 4-40 threaded set screws for placement in the tribometer. The gluing was done carefully with Loctite SuperGlue Gel so as not to contaminate the ruby surface.

Figure 13: 3mm Ruby Probe and 25mm PDMS Sample on Glass Window

C. Results & Discussion

C.1 Initial 1, 10, 100 Testing

The following figures are sourced from the raw adhesion data that is visible in the appendix.
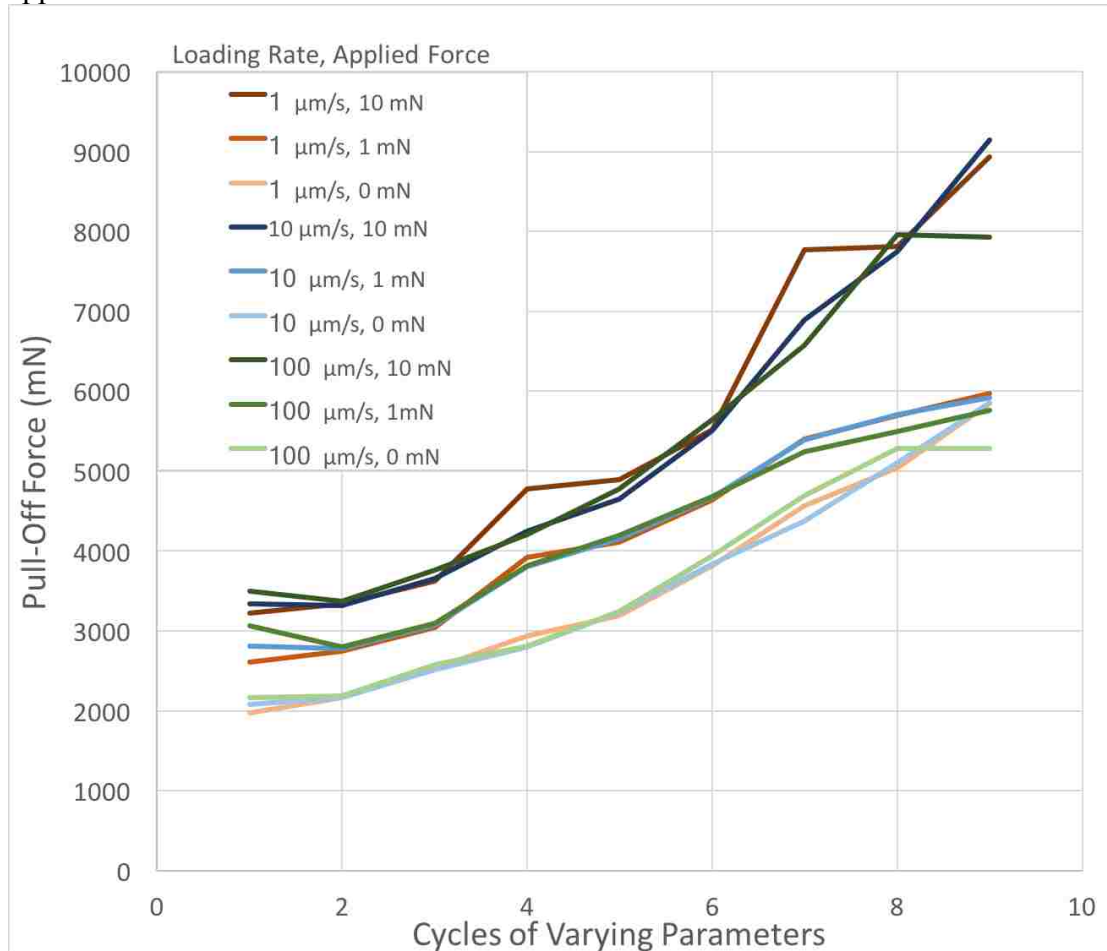

Figure 14: Effect of Loading rate on Pull-off Force

Each cycle value represents an individual indent, each with a different combination of parameters (i.e loading rate, dwell time, unloading rate, and applied load). The first varying parameter in our data collection is Loading rate, the speed at which the ruby indenter strikes the PDMS. The trend above shows adhesion force increasing as the testing parameters change. Each line represents a cycle of tests with the same unloading velocity but varying parameters of dwell time, loading rate and

applied load. Each color represents a loading rate. There are clearly 3 clusters of test cycles. Each cluster represents tests with the same applied force. From dark to light is 10mN, 1mN, and 0mN loads. The only varying parameter within these line clusters is loading rate.

Based on this analysis we can conclude that a varying loading rate has almost no effect on the final adhesive force. There are small variations within these clusters, so we theorize that the loading rate can be lumped into dwell time when investigation changes in adhesion force. The slower the loading rate, the longer the ruby and PDMS will be in contact before the dwell time even starts. This acts like a first dwell time that adds to the overall length of time that the surfaces are in contact. Further investigation into dwell time effects highlight the importance of distinction.
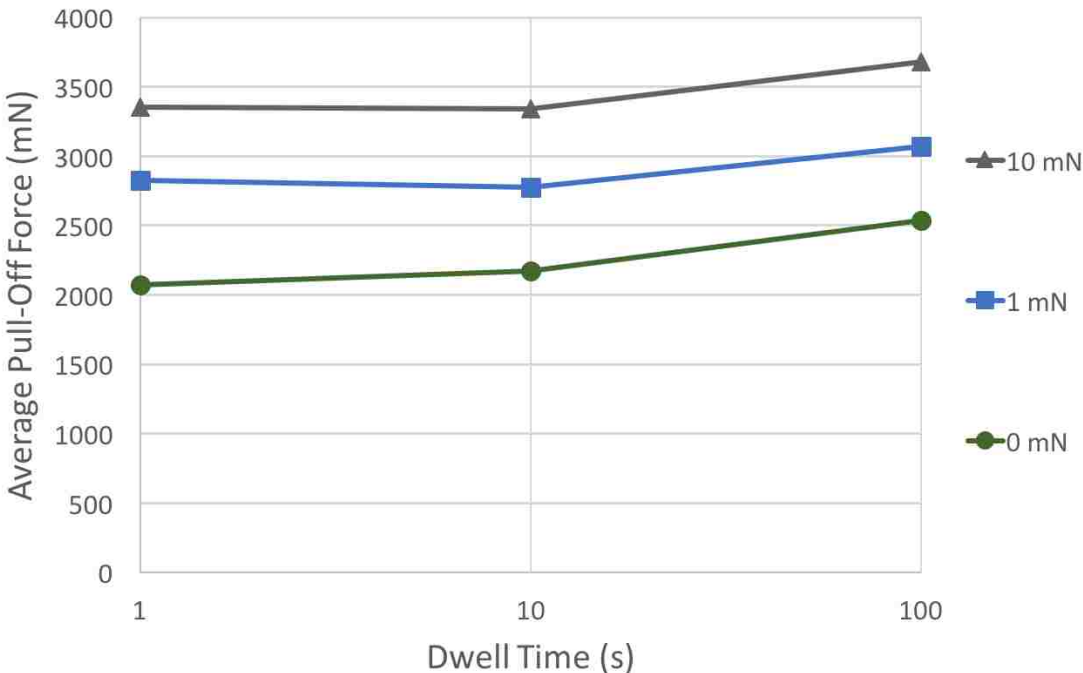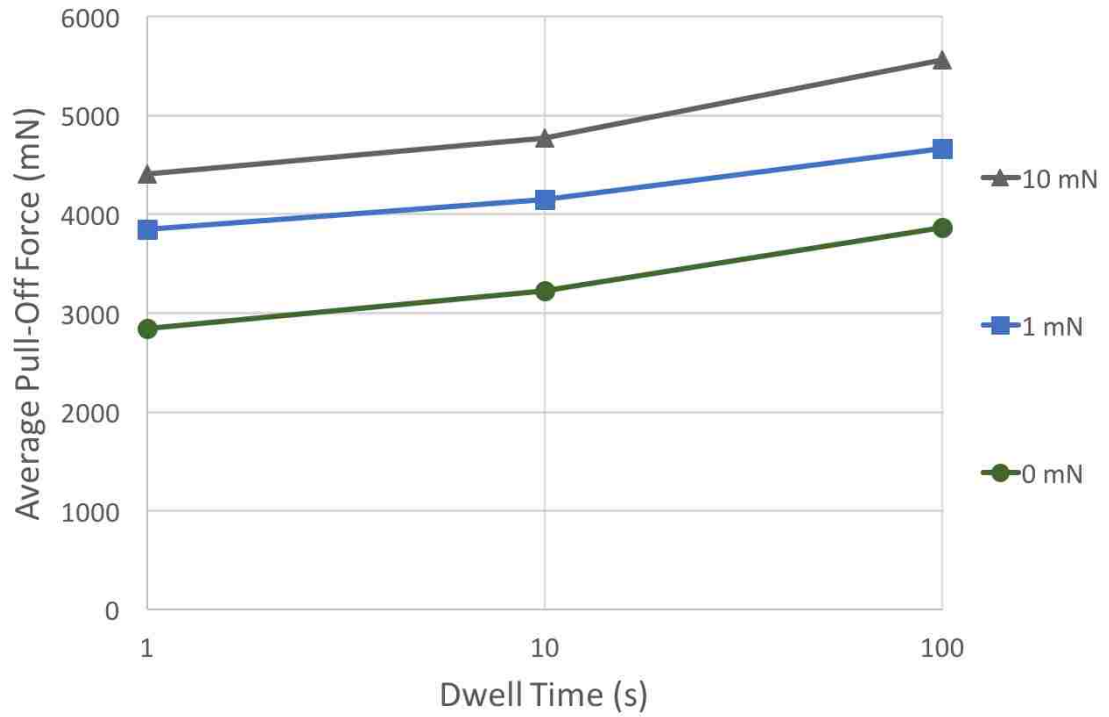

Figure 15: Effect of Dwell Time on *1 μm/s* Pull-off

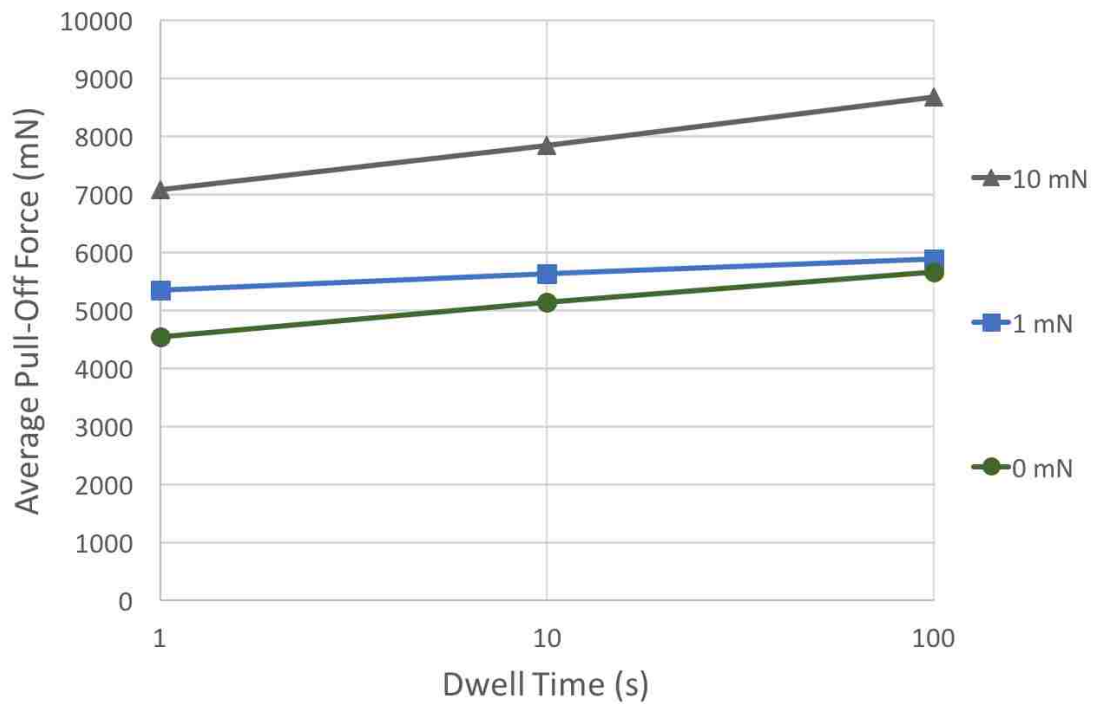**Figure 16: Effect of Dwell Time on *10 μm/*s Pull-off**

Figure 17: Effect of Dwell Time on *100 μm/*s Pull-off

Figures 13-15 show trends in dwell time vs pull-off force for varying loads and unloading speeds. Because the loading speeds seem to have no almost no correlation with pull-off force, tests with the same applied load have been averaged together for ease of viewing. Different colors represent different applied loads and the three plots group different unloading speeds together. In each plot a clear trend of increasing average pull-off force with increasing dwell time is clear. This trend is present in the literature as well and can be explained by a few different mechanisms.

The first effect to be aware of is that of fluid squeeze-out at the interface. Persson 2012[64] outlines the dynamics of fluid flow at the interface of elastic solids with rough surfaces. Environmental fluid (i.e. water, air, silicone oil, surface contaminants) is pushed out of the contact region as indentations take place and as the surfaces come together, energy is lost in squeezing fluid along the surface. In rough surfaces, fluid can get trapped among asperity regions preventing intimate contact and providing pressure that diminishes the adhesive force[65]. Such an analysis of fluid flow in the contact helps understand the relationship between loading rate and dwell time: faster loading speeds provide less time for fluid squeeze out than slower ones. Longer dwell times allow more time for the interface to develop intimate contact as asperities are compressed and fluid is expelled from regions between the two surfaces. In our case, longer contact allows for percolation of air, surface contaminants, and un-crosslinked silicone from the contact region.

A second closely related effect that is exhibited in contact of rubbers is surface bloom. Roberts & Othman 1997[66] prove the importance of dwell time to contact after extracting surface bloom from the surface of vulcanized rubbers. Longer dwell

times allow for the surfaces to effectively expel particles or other substances that have migrated to the surface from within the material. Our results are comparable to Choi 2008[67] who experimented with contact of a flat indenter and elastic rubbers. We believe the increase in adhesion force with increasing dwell time in our study is due to fluid/contaminant squeeze out and resultant growth of contact area.
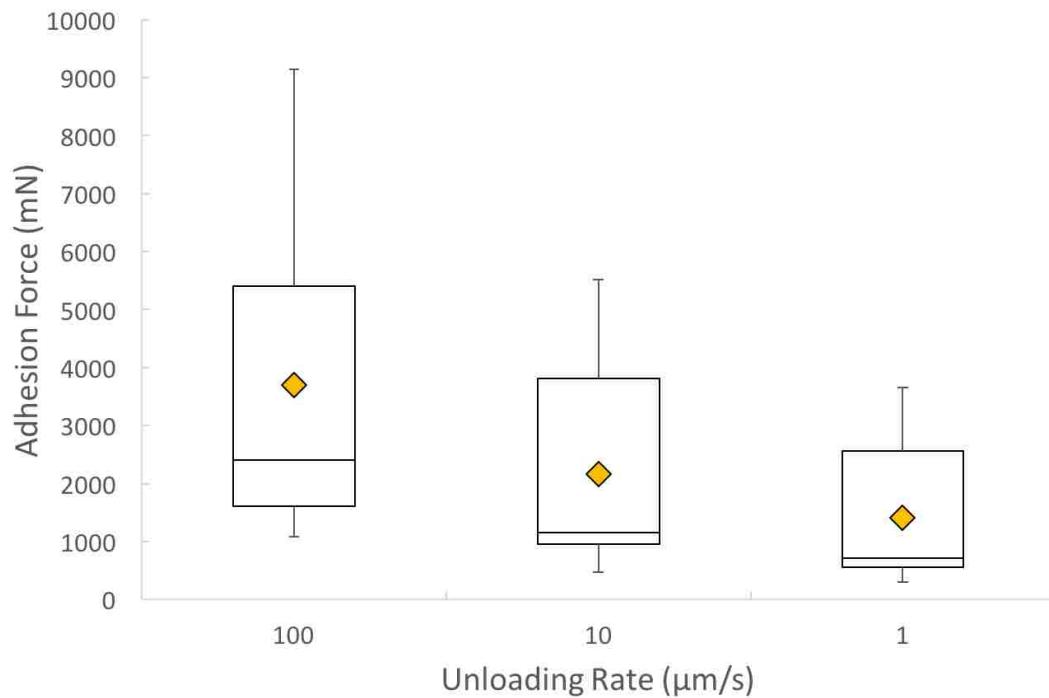

Figure 18: Effect of Unloading Rate on Pull-off Force

Due to the adhesive nature of the contact and viscoelasticity of the PDMS, unloading rate has a significant effect on pull-off force. Crack propagation in soft matter is a young field of study, but consistent results like these help verify current theories. The range of numbers in the 100 μm/s tests suggests that it is not unloading speed alone that contributes to increased pull-off force and that this rate has a more multiplicative effect on other parameters, namely contact area. This relationship can be viewed clearly in the next figure.
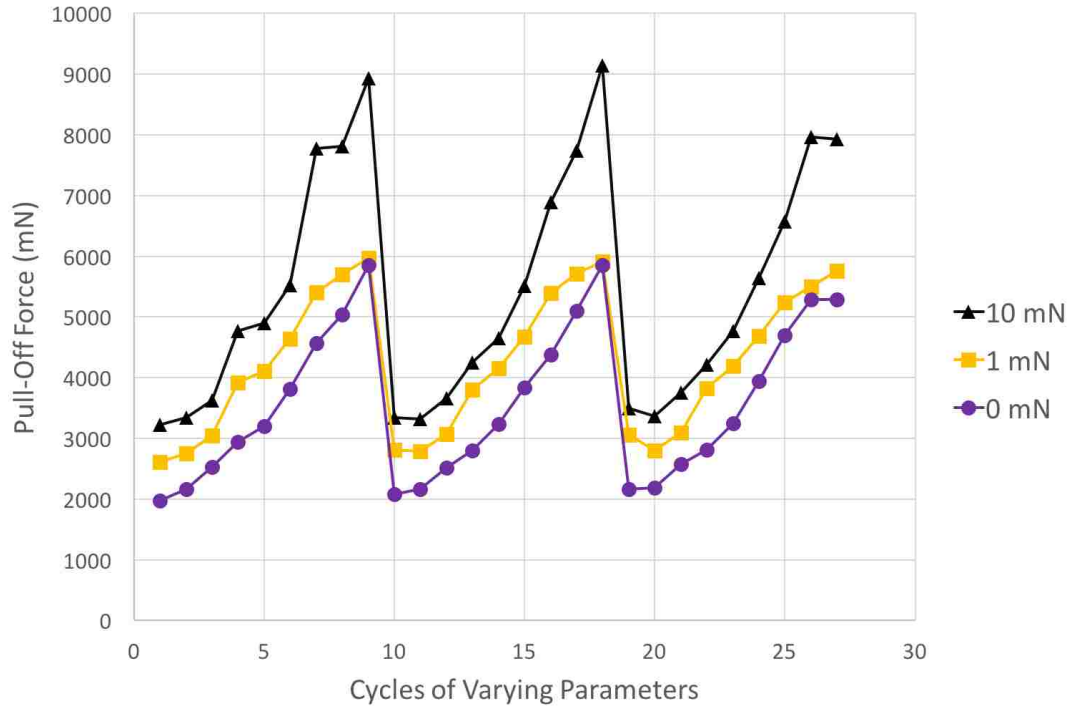
Figure 19: Effect of Load Pull-off Force

Each group of data above represents the evolution of pull-off forces through testing for a given load. The only constant in each of these datasets is applied force. The visible peaks are points where longest dwell times and fastest unloading rates meet, both of which have been shown to increase pull-off force.

This may be the least surprising data we have gathered. Increased load correlates with increased contact area and larger intimate contact means a greater adhesive force must be overcome to separate the two surfaces.

41

C.2 **In-Situ Contact Area Data**
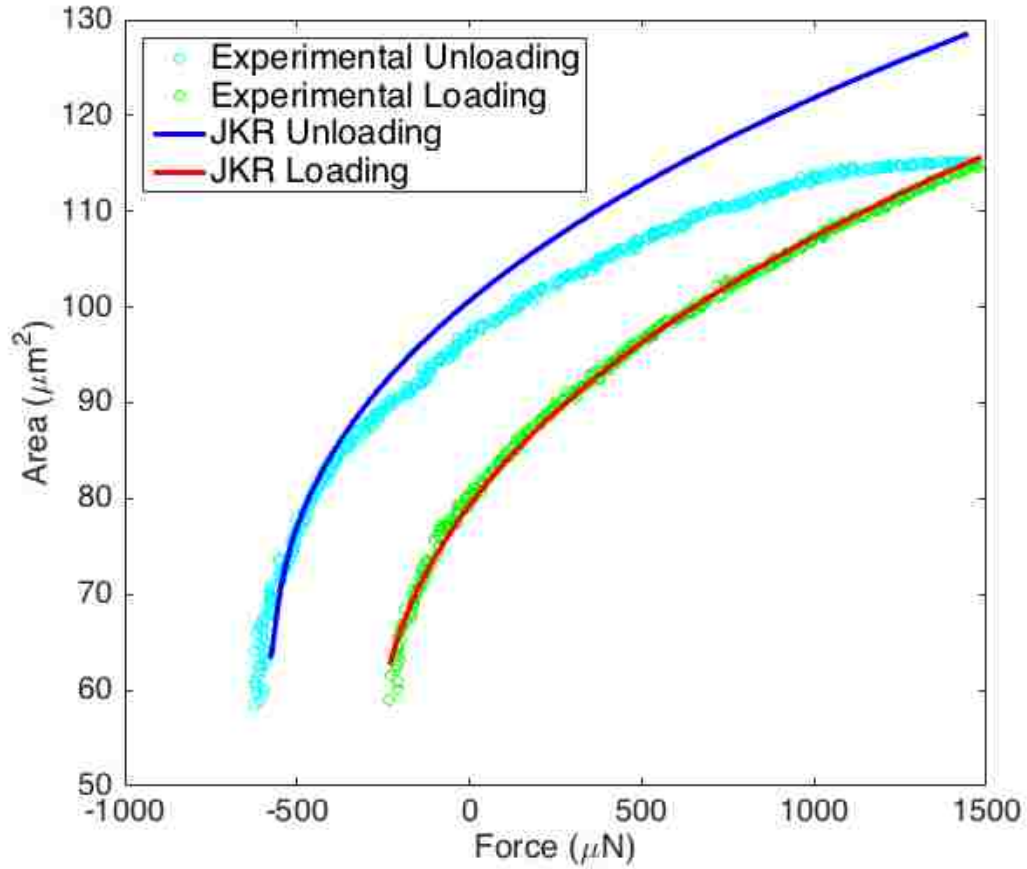
Figure 20: JKR fit on Area vs Force Adhesion Hysteresis Loop

Preliminary tests in the 1,10,100 testing cycles motivated further testing with in situ area measurements. The figure above shows a typical area vs force curves for adhesion hysteresis indentations. This test loaded to 1.5 mN. JKR theory fits exceptionally well to the loading regime.

$$a_{JKR}^3 = \frac{R}{K}\left(P + 3\pi\Delta\gamma R + [6\pi\Delta\gamma RP + (3\pi\Delta\gamma R)^2]^{\frac{1}{2}}\right)$$

The JKR fit predicts a modulus of 1.84 MPa, Poisson's ratio of 0.49, and work of adhesion(*combined surface energy $\Delta\gamma$*) of 39 mJ/m^2. These values are typical

for Sylgard 184 10:1. An exciting result is the work of adhesion which is consistent with results found in Silberzan *et al* 1994[46] and others.

JKR theory is incredibly accurate for basic loading at slow speeds but as expected, it doesn't hold up for the case of the unloading regime and falls apart in regard to adhesion hysteresis. Strong adhesion keeps the surfaces in contact during unload and viscoelasticity slows the reformation of the PDMS. The indenter pulls upwards quicker than the elastic restoration of the PDMS allows, spiking the pull-off force. Contact is only broken when the contact area is reduced to a point where the growing pull-off force can overcome the adhesion force.
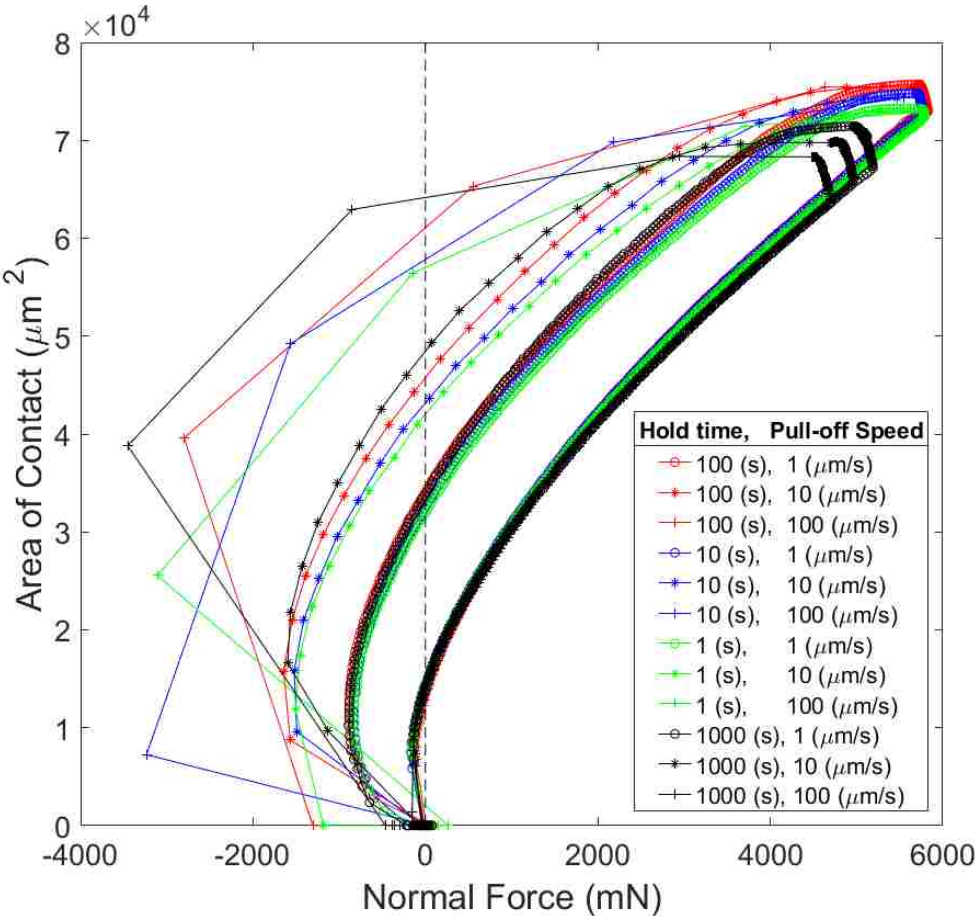

Figure 21: Full Adhesion Hysteresis Loops for Varying Parameters (A vs F)
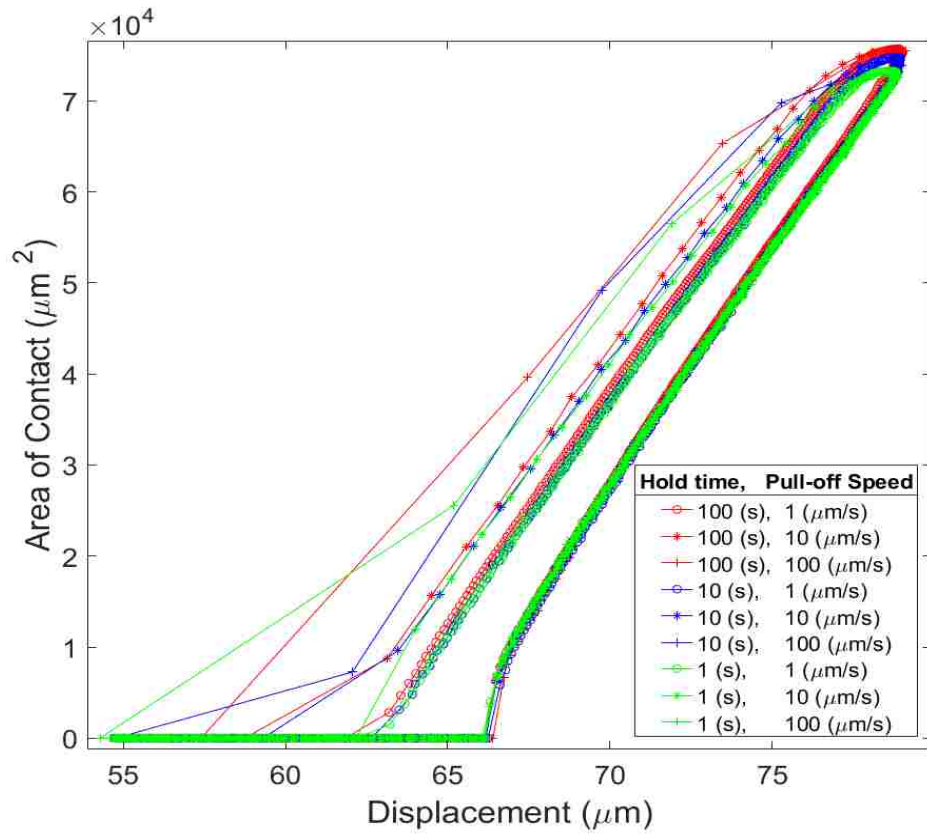
Figure 22: Full Adhesion Hysteresis Loops for Varying Parameters (A vs ∂)
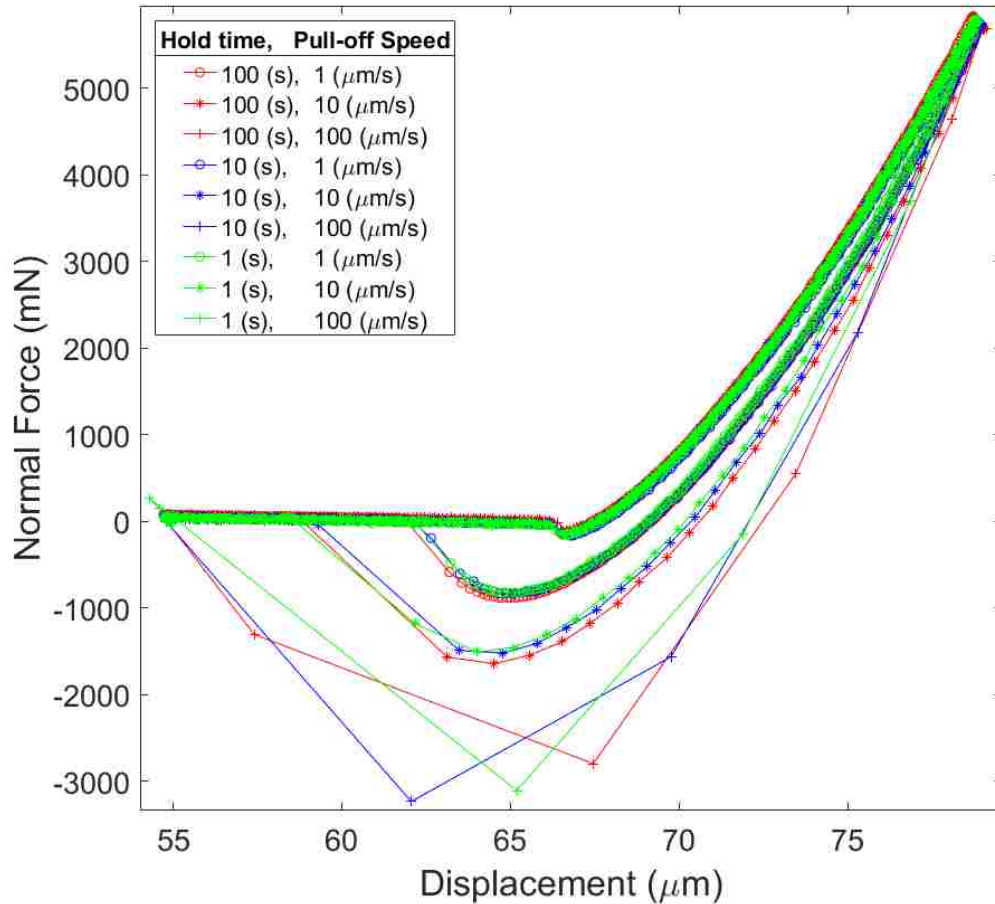
Figure 23: Full Adhesion Hysteresis Loops for Varying Parameters (F vs ∂)

Adhesion hysteresis is seen above as the loading regimes collapse in a single path while the unloading regimes show varying paths based on changing parameters. The loading regimes overlap as parameters there do not change. Applied Load(Normal Force) was kept relatively constant. Hysteresis increased significantly due to unloading rate(pull-off speed) and minimally with hold time. Rates of change of contact area with respect to displacement are identical for loading. A rate dependence is visible in unloading as contact area is maintained for longer distances with higher velocities. Below, further investigation is done with close-ups of the Area vs Force figure.
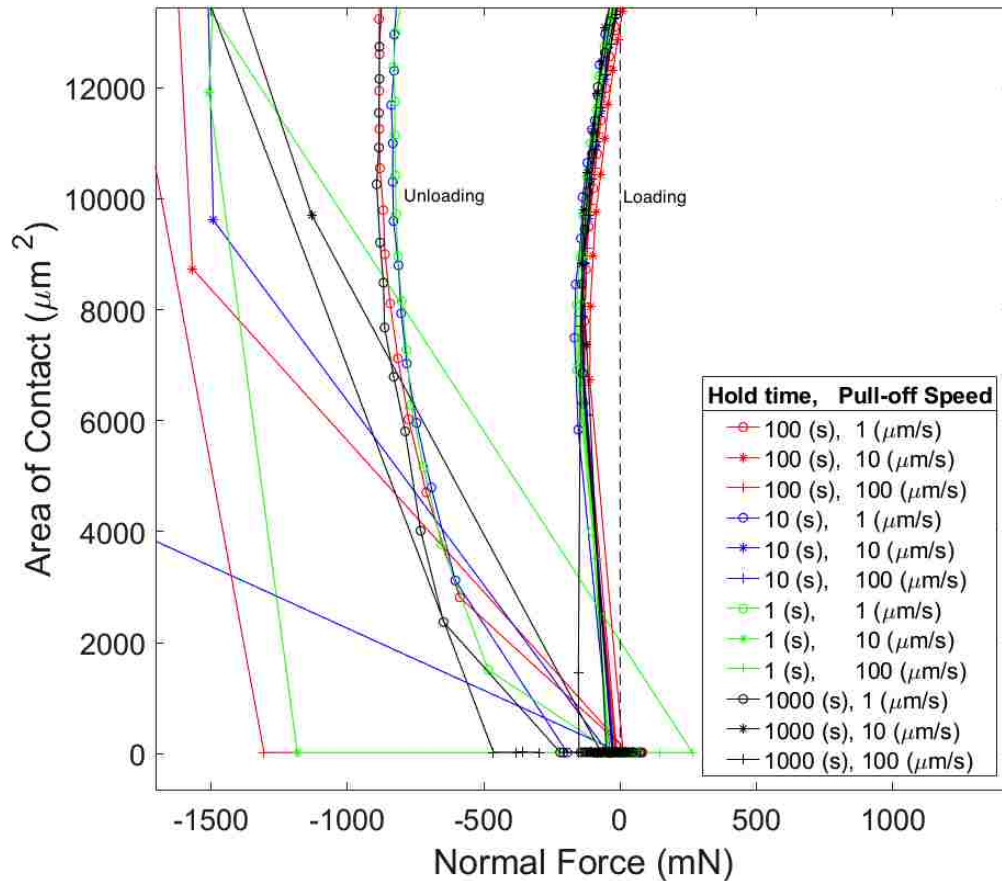
Figure 24: Bottom of Adhesion Hysteresis Loops for Varying Parameters

Here we see the beginning and end of the indenting cycles. There is noticeable adhesion upon initial contact shown by the negative jump on the x-axis as the ruby is pulled into the PDMS substrate. Normal force returns to a positive number as the z-stage catches up with the deflected cantilever and begins to apply a load. The unloading regimes reach significantly large negative loads before returning to their original positions as shown by the shallower slopes upon return. Positive values of load upon return are a result cantilever flexure after contact is broken and the indenter overshoots the zero position upon return. It is interesting to note the density of the data upon return. For the faster unloads, data is sparse because of the probe velocity.

46

The 1μm/s unloading regime shows larger areas of contact at larger negative loads than that of the initial contact, a perfect characterization of adhesion hysteresis. Because of intimate contact caused by loading, pulling apart the surfaces causes great strain in the PDMS, enough to shrink the contact area to about half of the initial contact area, before the force of unloading is great enough to overcome adhesion.
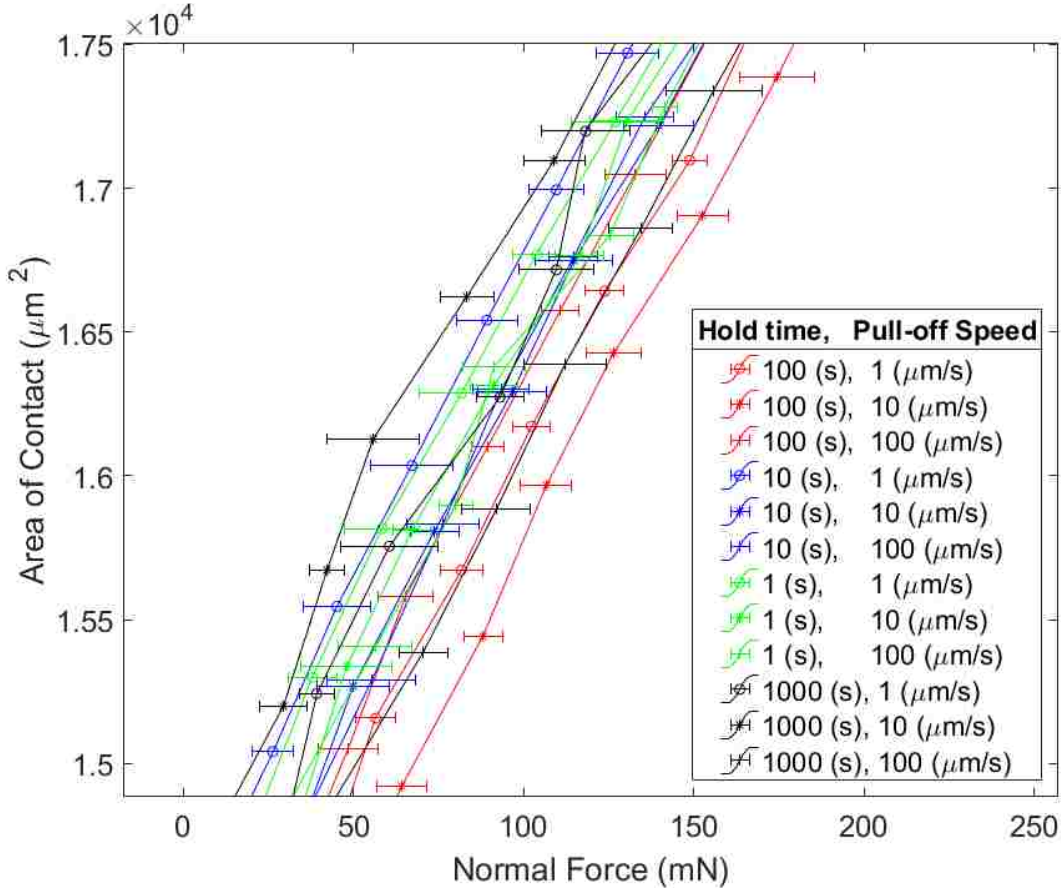
Figure 25: Loading Regime of Adhesion Hysteresis Loops

A close-up of the loading regime shows how tightly the different tests adhere to the same loading path. Discrepancies here are likely as much experimental error as they are actual changes in loading path.
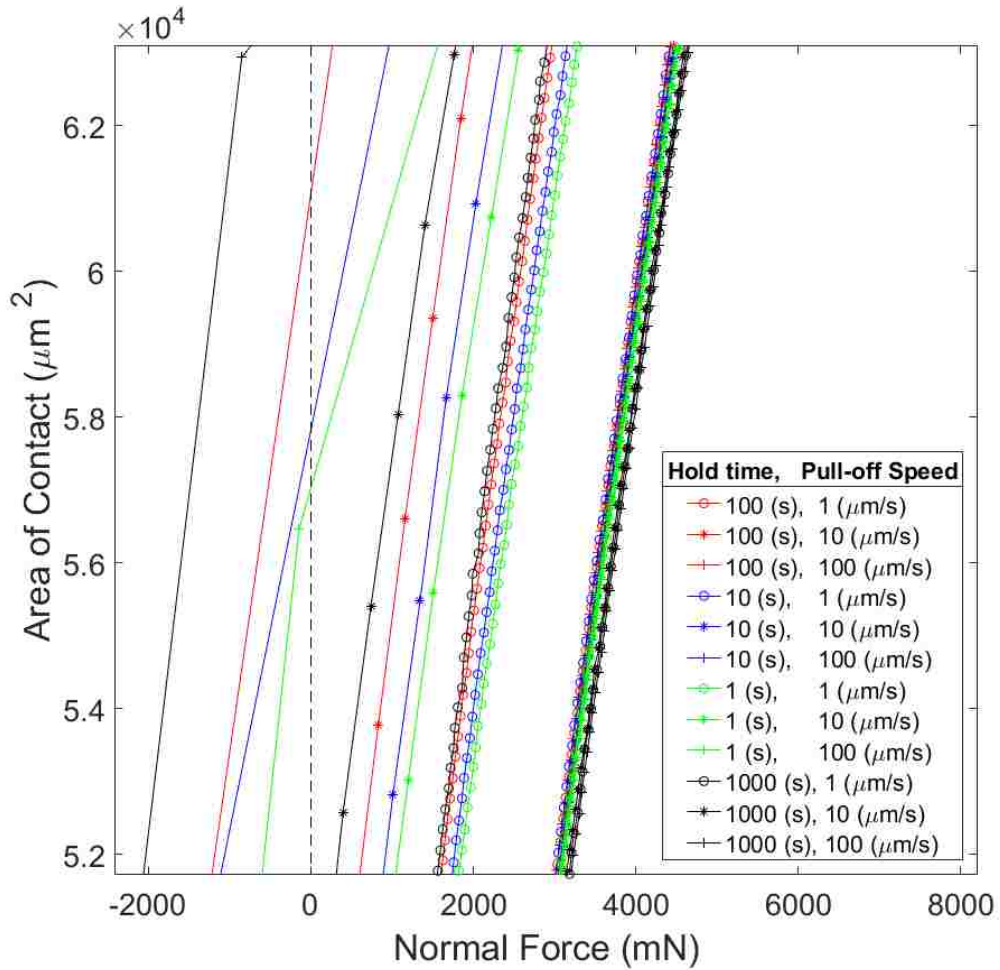
Figure 26: Middle of Adhesion Hysteresis Loops for Varying Parameters

A close-up on the middle of the loading and unloading regimes show a pattern of increasing pull-off force with increasing hold times and increasing unloading speeds. Each cluster of unloading data with the same pull off speed (i.e. circles, stars, crosses) contains the same pattern of indents with varying hold times. This further confirms the correlation of hold times with greater pull-off speeds. However, increasing pull-off speed increases pull-off force with respect to area at a greater rate than increasing dwell time, showing that overall contact area is far more important than how intimate the contact is.

48
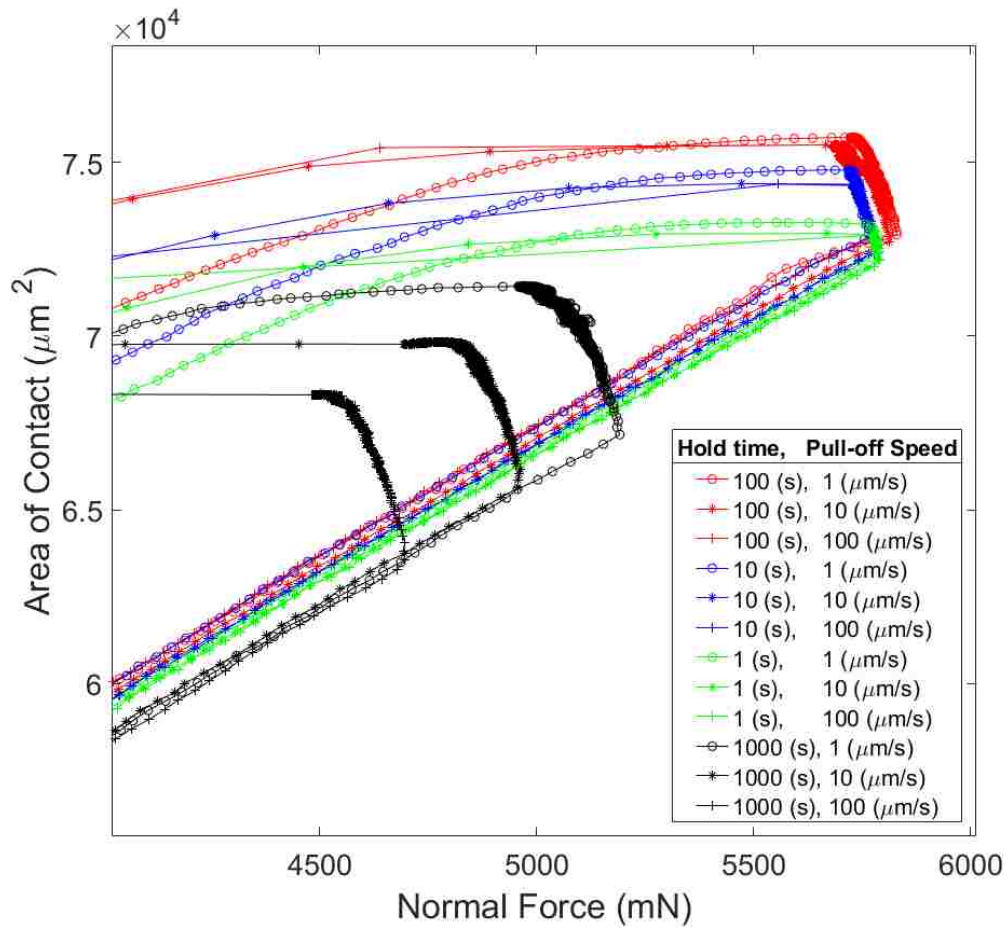
Figure 27: Top of Adhesion Hysteresis Loops for Varying Parameters

The dwell regimes are visible in the figure above. The 1, 10, and 100 second hold time tests were run consecutively attributing to their consistency. The 1000 second tests were run in a separate experiment due to limitations in computing for tests of such length. There is drift in the force channel causing the applied force in the long tests to change over time. Despite this, the shape of the adhesion hysteresis loops provides telling data about the behavior of the contact region.

Looking specifically at the 1 μm/s pull-offs(circles), it is evident how hold time ultimately changes the pull-off force. The probe reaches the desired applied force

and begins to settle into the PDMS substrate during dwell time, causing the area to increase and the applied force to decrease. This settling may be due to viscoelasticity and fluid squeeze-out. Notice that this slope is relatively constant in each indent despite the varying parameters, suggesting some sort of constant of viscoelastic settling based on material characteristics.

Traveling up this settling slope, we reach a max area for each indent. As the probe and PDMS stop settling and begin to sit comfortably in equilibrium contact at this point, data continues to write at the same speed causing the dense concentrations of points at the top of the hysteresis loops. In the 1000 second holds these dense lines reach the maximum area of the loop and then continue horizontally in the negative force direction. The force begins to drift in the negative direction but the area stays the same signifying that between 100 and 1000 seconds the contact becomes so intimate that negative forces upwards of 200mN have no immediate effect on the contact area.

C.3 **3D Tensile Zone Height Map Construction**
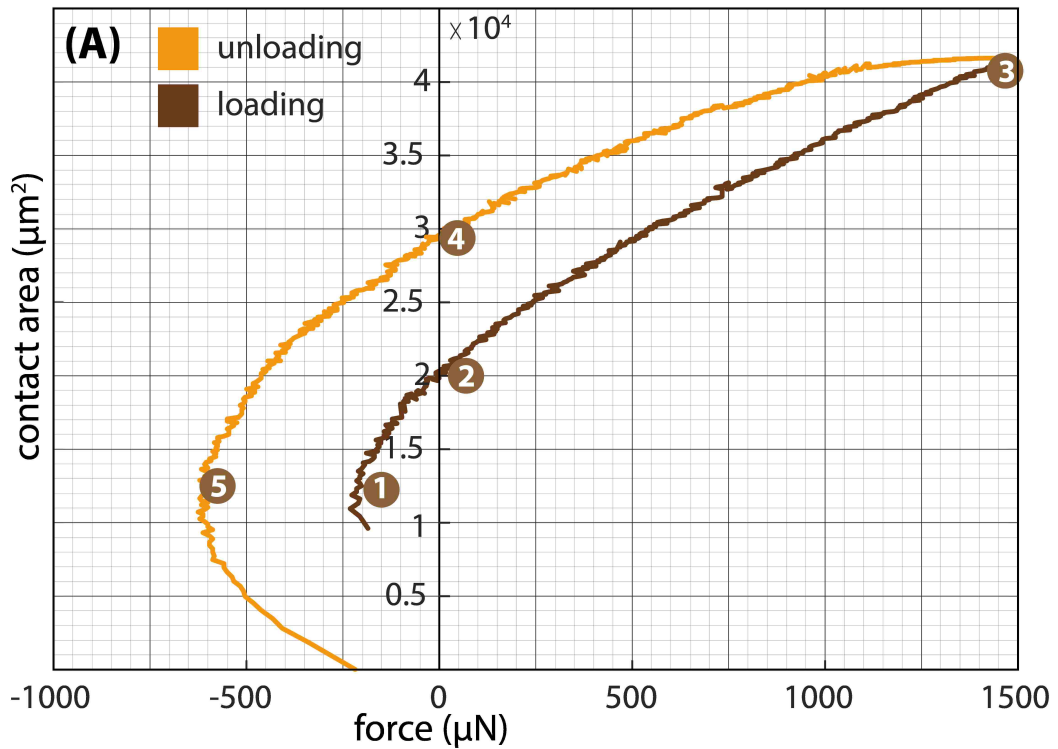

Figure 28: Adhesion Hysteresis Loop for 3D Modeling

The figure above shows the hysteresis loop of a 1.5 mN indent that corresponds to the following height maps. Numbered locations on the curve correspond to different height maps below.
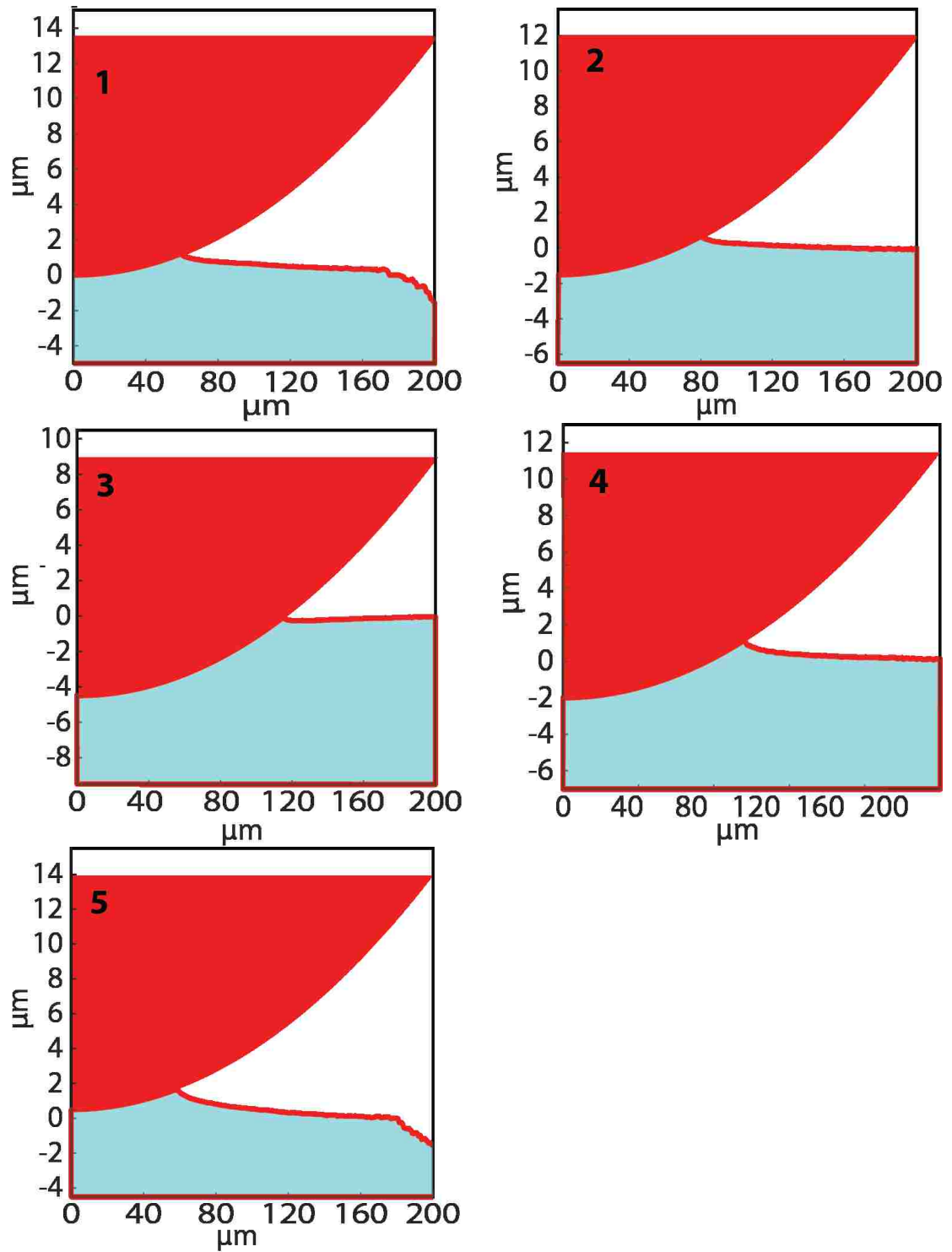
Figure 29: Five Height Maps Showing Evolution of the Tensile Zone

The height maps and 3D model have been distorted in the y-direction considerably to allow for viewing of relative changes in the tensile zone. Data is no longer reliable after 160 μm in the radial direction due to size and clarity of fringes that far out. A solid meniscus, or tensile zone, was observed for all indentation forces (adhesive and compressive). Consistency in geometry was observed between all loads modeled using this technique. The following numbered descriptions correspond to the number on each height map and on the hysteresis loop.

1. The Ruby ball and PDMS surface snapped into contact due to adhesive forces. The silicone surface was pulled up to the ball, resulting in relatively large tensile region and a negative load.

2. Balance between compressive and tensile (adhesive) energies resulted in zero externally applied load. Contact area continued to grow with increasing applied load. The tensile zone was small.

3. The normal load of 1.5 mN causes a downward deformation of the silicone. However, a small tensile zone persisted where the PDMS was adhered to the ruby surface. Dwell resulted in intimate contact.

4. The force between tensile zone and pull-off was equal, but there was a significant increase in tensile zone height due to bulk viscoelasticity. The ball began to unload quickly, and adhesion hysteresis caused the contact area to be larger than at the previous equilibrium position.

5. At pull-off(max adhesive force), the ruby position was above zero, the contact are was small, and the tensile zone was very large in both height and width.
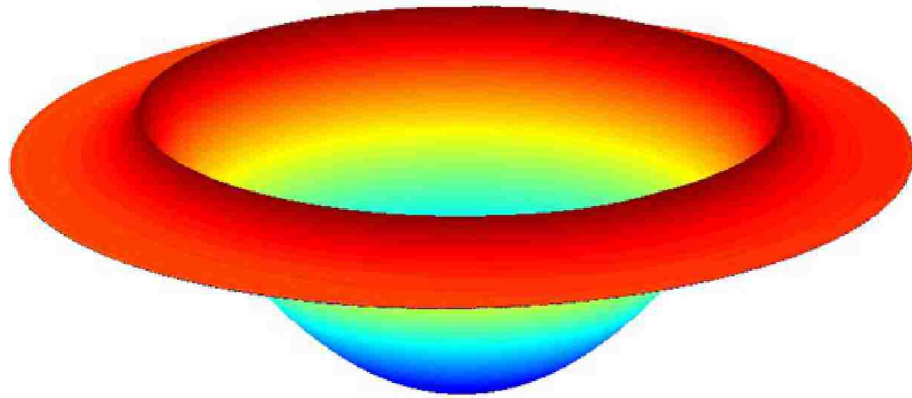
Figure 30: 3D Model of the PDMS Surface in the Tensile Region
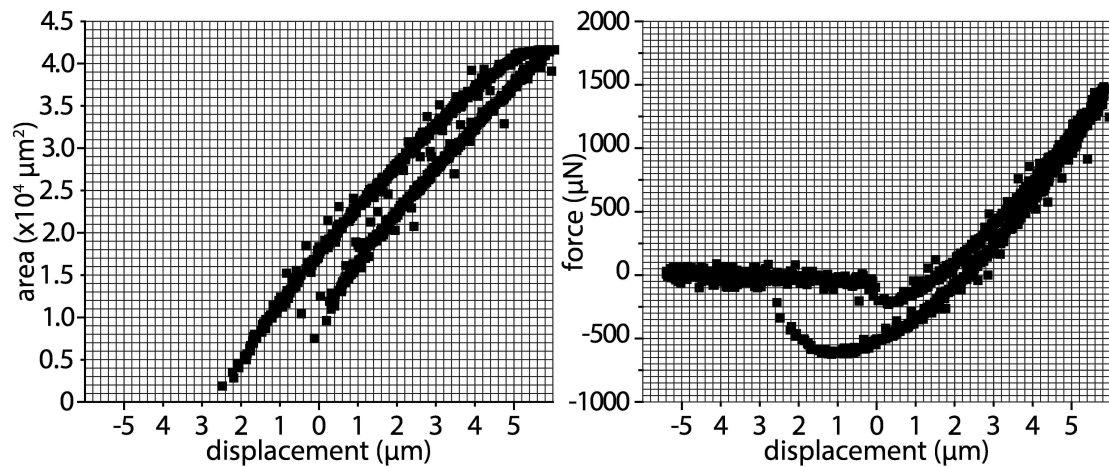
Figure 31: Area vs Displacement & Force vs Displacement Plots

The Area vs Displacement plot helps reinforce statements about the behavior of the tensile zone. For the most part, contact area increased linearly as displacement increased, except at the beginning of pull-off. In this region, the displacement decreased with decrease in force, while contact area remained relatively stable due strong adhesion formed through intimate contact. The contact area eventually began to reduce in an inverse fashion as the loading phase. The force vs displacement plot shows measureable negative forces upon approach and upon unload as expected based on area vs force plots.
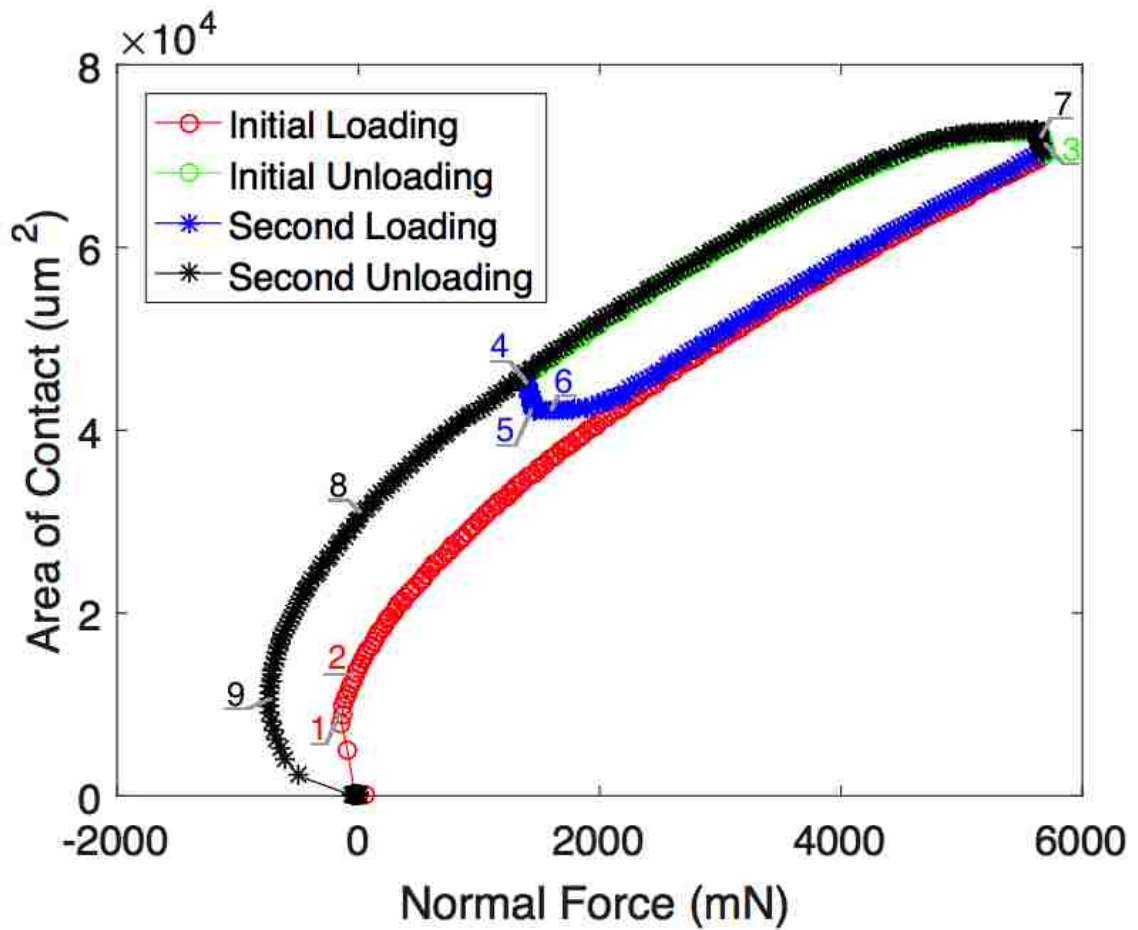
Figure 32: Area Vs Force of Two Indents Without Breaking Contact

Tests were run to explore hysteretic behavior of indents where there was no break in contact. In these cases, an initial load was applied and then subsequent loads were reached without fully removing the ruby from contact with the PDMS. The figure above shows one such test. All loading and unloading for this test was done at 1 μm/s, and all dwell times were 10 seconds. Initial load was about 5 mN and the second load was 1.5 mN.

Initial loading and unloading follow the expected path based on prior experimentation. Interesting behavior begins to happen at the second dwell time(blue

star). At this point, area drops with no change in force. You'll notice that this drop in area is at a similar rate and slope as the increase in area seen at the initial dwell time. It appears that the viscoelastic effects acting at the dwell times are the same in either direction. In all cases of testing, the second dwell time brought the path of the hysteresis loop down to the original loading path. The longer the second dwell time, the closer the path will get to the original loading path. Upon second loading, the loading paths meet and the same hysteresis loop is traced out again.

Full size height maps corresponding to the numbers on Figure 32 can be viewed in Appendix 2. Below, the tensile zone at each location is described:

1. This is first contact. Notice the ruby/PDMS interface is at a height of zero. There is a visible tensile region due to adhesion.

2. At zero load, the ruby/PDMS interface is below the point of initial contact. The PDMS sucks in the sphere and the tensile zone persists.

3. At load, the ruby is fully indented. Deformation of the bulk PDMS is apparent, as the surface outside of contact is visibly deformed. The tensile region persists despite the load as it can be seen climbing up to ball.

4. Less bulk deformation is visible with the decreased load and the tensile region remains about the same size.

5. The tensile region remains during dwell time as indentation depth remains relatively the same.

6. Deformation is visible upon loading and the tensile zone seems to have lost its peak. Additional force seems to have no effect on contact area in this regime,

instead deforming the tensile zone until the force/area ratio reaches that of the loading regime.

7. The second dwell period (5mN) shows no considerable difference from the first.

8. Zero load on unloading has a much larger tensile zone than zero load on loading.

9. The PDMS surface is pulled upwards resulting in large tensile region with small contact area.

D. <u>Conclusions</u>

When indenting Ruby into PDMS, contact is initialized by attractive forces between the surfaces that are observed as a negative load on the cantilever. Varying adhesive forces are a product of different loading rates, dwell times, unloading rates, and applied loads. Unloading rates and dwell times can be considered one parameter, as both affect total contact time before pull-off, which increases adhesive force. In the future, loading rate can remain constant and the adhesion force can be evaluated solely as a function of dwell time. Longer dwell times lead to higher adhesive forces due to enhanced bonding at the interface, in part, by ample time for fluid to squeeze out. This effect is independent of the loading rate and applied force. Area continues to grow during contact, despite constant load, due to settling and other factors. At load, an equilibrium is reached where small negative variations in force have no noticeable effect on contact area. In order to lower the area of contact between the two surfaces in contact, the applied force must be significantly reduced. Another critical force is

reached at pull-off, the max adhesion force, that corresponds to the critical area before separation.

Increasing unloading rate will increase adhesion force. The reason for this phenomenon is still not entirely understood, but the results are consistent with previous experimentation in showing rate dependence. Crack tip velocity is limited due to viscoelasticity at the surface and in the bulk material. Faster unloading may allow for greater forces to be reached before the contact area can adjust with an equal but opposite adhesive force. Higher loads result in larger adhesion forces. Greater contact area due to greater deformation results in more bonds at the interface and more area for dispersive adhesion, which both contribute to the energy required to break contact.

Newton Rings captured in images of contact were used successfully to create height maps and three dimensional models of the tensile region. The models show that the tensile region is always present during contact, even during loading and when the substrate deforms under the applied load. Local adhesion at the interface is so large that the solid PDMS meniscus will remain during increased loading. The changing load instead effects bulk deformation and overall contact area. This meniscus is only reduced during a second loading, after in-contact unloading. The additional load causes a transition at the surface as the system returns to the loading regime from the unloading regime. Separately, the tensile region grows during unloading, as local adhesion forces increase.

E. <u>Future Work</u>

This work provides the foundation for an endless amount of other experimentation in adhesion. In the current set-up, high speed unloading rates present a challenge to the imaging system which can only reasonably acquire at 8 fps. A high-speed camera would not only provide better data for plots, but also better data for tensile zone reconstruction. There are critical points where strong adhesive contact begins to peel and where contact seizes entirely that would be possible to image with such a setup, allowing for assignment of critical contact area. In the same realm, using multiple monochromatic light sources could potentially help provide more accurate 3D models. During the times where there is compression and tension, using two separate wavelengths can help find if there are any ripples in the surface through comparing fringe patterns.

The LISOT is designed to provide opportunities for environmental testing, a logical next step. Tiwari *et al* 2017[68] have shown interesting results for indents submerged in water and acetone, while Persson 2012[64] offered implications for fluid squeeze out. Removing any fluid altogether (i.e. vacuum) and creating a completely dust free environment would provide a strong data for effects of fluid squeeze out and contaminants at the surface. Future experimentation might also look at what specific parameters effect the geometry of the tensile region and attempt to create model for the surface based on their findings.

F. <u>Vita</u>

Michael Sedaille was born on July 30th, 1993 to Lori Ann and Dennis Sedaille in Belleville, NJ, USA and grew up in Cedar Grove NJ, USA. He received his Bachelor of Arts in Physics and Math from Drew University in Madison, NJ in the spring of 2015. The following fall he began pursuing a Master of Science in Mechanical Engineering at Lehigh University and will graduate in the summer of 2017.

References

[1]   J. Li, H. Chen, and H. a Stone, "Ice lubrication for moving heavy stones to the Forbidden City in 15th- and 16th-century China.," *Proc. Natl. Acad. Sci. U. S. A.*, vol. 110, no. 50, pp. 20023–7, 2013.

[2]   S. Q. Liu, R. Tay, M. Khan, P. L. Rachel Ee, J. L. Hedrick, and Y. Y. Yang, "Synthetic hydrogels for controlled stem cell differentiation," *Soft Matter*, vol. 6, no. 1, p. 67, 2010.

[3]   M. F. Maitz, "Applications of synthetic polymers in clinical medicine," *Biosurface and Biotribology*, vol. 1, no. 3, pp. 161–176, 2015.

[4]   D. W. Hutmacher, "Scaffolds in tissue engineering bone and cartilage.," *Biomaterials*, vol. 21, no. 24, pp. 2529–2543, 2000.

[5]   H. N. Chia and B. M. Wu, "Recent advances in 3D printing of biomaterials," *J. Biol. Eng.*, vol. 9, p. 4, 2015.

[6]   J. S. Marshall, "Discrete-element modeling of particulate aerosol flows," *J. Comput. Phys.*, vol. 228, no. 5, pp. 1541–1561, 2009.

[7]   S. M. Albelda and C. A. Buck, "Integrins and other cell adhesion molecules," *FASEB J.*, vol. 4, no. 11, 1990.

[8]   R. C. Tolman, "The effect of droplet size on surface tension," *J. Chem. Phys.*, vol. 17, no. 3, 1949.

[9]   K. L. Johnson, "Contact Mechanics," *Contact Mech.*, 1985.

[10]   B. N. J. Persson, O. Albohr, U. Tartaglino, A. I. Volokitin, and E. Tosatti, "On the nature of surface roughness with application to contact mechanics, sealing, rubber friction and adhesion," *J. Phys. Condens. Matter*, vol. 17, no. 1, 2005.

[11]   M. K. Chaudhury and G. M. Whitesides, "Direct measurement of interfacial interactions between semispherical lenses and flat sheets of poly(dimethylsiloxane) and their chemical derivatives," *Langmuir*, vol. 7, no. 5, pp. 1013–1025, 1991.

[12]   K. Autumn and A. M. Peattie, "Mechanisms of adhesion in geckos.," *Integr. Comp. Biol.*, vol. 42, no. 6, pp. 1081–1090, 2002.

[13]   C. H. Mastrangelo, "Adhesion-related failure mechanisms in micromechanical devices," *Tribol. Lett.*, vol. 3, no. 3, 1997.

[14]   F. J. Giessibl, "Advances in atomic force microscopy," *Rev. Mod. Phys.*, vol.

75, no. 3, pp. 949–983, 2003.

[15] H. J. Butt, B. Cappella, and M. Kappl, "Force measurements with the atomic force microscope: Technique, interpretation and applications," *Surf. Sci. Rep.*, vol. 59, no. 1–6, pp. 1–152, 2005.

[16] J. Erath, S. Schmidt, and A. Fery, "Characterization of adhesion phenomena and contact of surfaces by soft colloidal probe AFM," *Soft Matter*, vol. 6, no. 7, p. 1432, 2010.

[17] K. L. Johnson, K. Kendall, and A. D. Roberts, "Surface Energy and the Contact of Elastic Solids," *Proc. R. Soc. A Math. Phys. Eng. Sci.*, vol. 324, no. 1558, pp. 301–313, 1971.

[18] X. Shi and Y.-P. Zhao, "Comparison of various adhesion contact theories and the influence of dimensionless load parameter," *J. Adhes. Sci. Technol.*, vol. 18, no. 1, pp. 55–68, 2004.

[19] K. Kendall, "The adhesion and surface energy of elastic solids," *J. Phys. D. Appl. Phys.*, vol. 4, no. 8, pp. 1186–1195, 2002.

[20] B. V Derjaguin, V. M. Muller, and Y. U. P. Toporov, "Effect of contact deformation on the adhesion of particles.," *J. Colloid Interface Sci.*, vol. 52, no. 3, pp. 105–108, 1975.

[21] B. Dahneke, "The influence of flattening on the adhesion of particles," *J. Colloid Interface Sci.*, vol. 40, no. 1, pp. 1–13, 1972.

[22] R. S. Bradley, "The Cohesion Between Smoke Particles," *Trans. Faraday Soc.*, no. 32, pp. 1088–1090, 1936.

[23] D. Tabor, "Surface forces and surface interactions," *J. Colloid Interface Sci.*, vol. 58, no. 1, pp. 2–13, 1977.

[24] V. M. Muller, V. S. Yushchenko, and B. V. Derjaguin, "On the influence of molecular forces on the deformation of an elastic sphere and its sticking to a rigid plane," *Prog. Surf. Sci.*, vol. 45, no. 1–4, pp. 157–167, 1994.

[25] D. Maugis, "Adhesion of spheres: The JKR-DMT transition using a dugdale model," *J. Colloid Interface Sci.*, vol. 150, no. 1, pp. 243–269, 1992.

[26] I. N. Sneddon, "The relation between load and penetration in the axisymmetric boussinesq problem for a punch of arbitrary profile," *Int. J. Eng. Sci.*, vol. 3, no. 1, pp. 47–57, May 1965.

[27] R. W. Carpick, D. F. Ogletree, and M. Salmeron, "A general equation for fitting contact area and friction vs load measurements," *J. Colloid Interface Sci.*, vol.

211, no. 2, 1999.

[28] K. L. Johnson and J. A. Greenwood, "An adhesion map for the contact of elastic spheres," *J. Colloid Interface Sci.*, vol. 192, no. 2, 1997.

[29] U. D. Schwarz, "A generalized analytical model for the elastic deformation of an adhesive contact between a sphere and a flat surface," *J. Colloid Interface Sci.*, vol. 261, no. 1, pp. 99–106, 2003.

[30] O. Piétrement and M. Troyon, "General Equations Describing Elastic Indentation Depth and Normal Contact Stiffness versus Load.," *J. Colloid Interface Sci.*, vol. 226, pp. 166–171, 2000.

[31] E. Barthel, "Adhesive elastic contacts: JKR and more," *J. Phys. D. Appl. Phys.*, vol. 41, no. 16, p. 163001, 2008.

[32] M. Morales-Hurtado, E. G. de Vries, M. Peppelman, X. Zeng, P. E. J. van Erp, and E. van der Heide, "On the role of adhesive forces in the tribo-mechanical performance of ex vivo human skin," *Tribol. Int.*, vol. 107, 2017.

[33] J. Joe, M. Scaraggi, and J. R. Barber, "Effect of fine-scale roughness on the tractions between contacting bodies," *Tribol. Int.*, vol. 111, 2017.

[34] C. Creton and M. Ciccotti, "Fracture and adhesion of soft materials: a review," *Reports Prog. Phys.*, vol. 79, no. 4, p. 46601, 2016.

[35] B. A. Krick, J. R. Vail, B. N. J. Persson, and W. G. Sawyer, "Optical In Situ Micro Tribometer for Analysis of Real Contact Area for Contact Mechanics, Adhesion, and Sliding Experiments," *Tribol. Lett.*, vol. 45, no. 1, pp. 185–194, 2012.

[36] R. R. Chromik, C. C. Baker, A. A. Voevodin, and K. J. Wahl, "In situ tribometry of solid lubricant nanocomposite coatings," *Wear*, vol. 262, no. 9–10, pp. 1239–1252, 2007.

[37] K. J. Wahl, R. R. Chromik, and G. Y. Lee, "Quantitative in situ measurement of transfer film thickness by a Newton's rings method," *Wear*, vol. 264, no. 7–8, pp. 731–736, 2008.

[38] C. W. McCutchen, "Optical systems for observing surface topography by frustrated total internal reflection and by interference," *Rev. Sci. Instrum.*, vol. 35, no. 10, pp. 1340–1345, 1964.

[39] W. G. Sawyer and K. J. Wahl, "Accessing Inaccessible Interfaces: In Situ Approaches to Materials Tribology," *MRS Bull.*, vol. 33, no. 12, pp. 1145–1150, 2008.

[40] B. Lorenz *et al.*, "Adhesion: role of bulk viscoelasticity and surface roughness.," *J. Phys. Condens. Matter*, vol. 25, no. 22, p. 225004, 2013.

[41] B. N. J. Persson and M. Scaraggi, "Theory of adhesion: Role of surface roughness," *J. Chem. Phys.*, vol. 141, no. 12, 2014.

[42] B. N. J. Persson, "Theory of rubber friction and contact mechanics," *J. Chem. Phys.*, vol. 115, no. 8, 2001.

[43] L. Dorogin, A. Tiwari, C. Rotella, P. Mangiagalli, and B. ?N. ?J. Persson, "Role of Preload in Adhesion of Rough Surfaces," *Phys. Rev. Lett.*, vol. 118, no. 23, p. 238001, 2017.

[44] B. N. J. Persson, O. Albohr, G. Heinrich, and H. Ueba, "Crack propagation in rubber-like materials," *J. Phys. Condens. Matter*, vol. 17, no. 44, pp. R1071–R1142, 2005.

[45] M. K. CHAUDHURY and G. M. WHITESIDES, "Correlation Between Surface Free Energy and Surface Constitution," *Science*, vol. 255, no. 5049. pp. 1230–1232, 1992.

[46] P. Silberzan, S. Perutz, E. J. Kramer, and M. K. Chaudhury, "Study of the Self-Adhesion Hysteresis of a Siloxane Elastomer Using the JKR Method," *Langmuir*, vol. 10, no. 6, pp. 2466–2470, 1994.

[47] M. Ruths and S. Granick, "Rate-dependent adhesion between polymer and surfactant monolayers on elastic substrates," *Langmuir*, vol. 14, no. 7, pp. 1804–1814, 1998.

[48] C. Kovalchick, A. Molinari, and G. Ravichandran, "Rate Dependent Adhesion Energy and Nonsteady Peeling of Inextensible Tapes," *J. Appl. Mech.*, vol. 81, no. 4, p. 41016, 2013.

[49] K. Vorvolakos and M. K. Chaudhury, "The effects of molecular weight and temperature on the kinetic friction of silicone rubbers," *Langmuir*, vol. 19, no. 17, pp. 6778–6787, 2003.

[50] M. K. Chaudhury and K. H. Kim, "Shear-induced adhesive failure of a rigid slab in contact with a thin confined film," *Eur. Phys. J. E*, vol. 23, no. 2, pp. 175–183, 2007.

[51] A. Ghatak, K. Vorvolakos, H. She, D. L. Malotky, and M. K. Chaudhury, "Interfacial Rate Processes in Adhesion and Friction," *J. Phys. Chem. B*, vol. 104, no. 17, pp. 4018–4030, 2000.

[52] A. Jagota and S. J. Bennison, "Mechanics of Adhesion Through a Fibrillar Microstructure 1," *Integr. Comp. Biol*, vol. 42, pp. 1140–1145, 2002.

[53] M. Mori, B. J. Crain, V. P. Chacko, and P. C. M. Van Zijl, "Three-dimensional tracking of axonal projections in the brain by magnetic resonance imaging," *Ann. Neurol.*, vol. 45, no. 2, 1999.

[54] S. Helveg *et al.*, "Atomic-scale imaging of carbon nanofibre growth," *Nature*, vol. 427, no. 6973, 2004.

[55] A. Das *et al.*, "Monitoring dopants by Raman scattering in an electrochemically top-gated graphene transistor," *Nat. Nanotechnol.*, vol. 3, no. 4, 2008.

[56] E. Kroner, R. Maboudian, and E. Arzt, "Adhesion characteristics of pdms surfaces during repeated pull-off force measurements," *Adv. Eng. Mater.*, vol. 12, no. 5, 2010.

[57] E. Centre, F. O. R. Ecotoxicology, and T. O. F. Chemicals, "Linear Polydimethylsiloxanes CAS No. 63148-62-9 (Second Edition)," vol. 9, no. 63148.

[58] I. D. Johnston, D. K. McCluskey, C. K. L. Tan, and M. C. Tracey, "Mechanical characterization of bulk Sylgard 184 for microfluidics and microengineering," *J. Micromechanics Microengineering*, vol. 24, p. 35017, 2014.

[59] J. C. Lötters, W. Olthuis, P. H. Veltink, and P. Bergveld, "The mechanical properties of the rubber elastic polymer polydimethylsiloxane for sensor applications," *J. Micromechanics Microengineering*, vol. 7, no. 3, pp. 145–147, 1999.

[60] J. E. Mark, "Polymer Data Handbook," *Oxford Univ. Press*, 1999.

[61] A. Mata, A. J. Fleischman, and S. Roy, "Characterization of polydimethylsiloxane (PDMS) properties for biomedical micro/nanosystems.," *Biomed. Microdevices*, vol. 7, no. 4, 2005.

[62] A. B. Mathur *et al.*, "In vivo biocompatibility and biostability of modified polyurethanes," *J. Biomed. Mater. Res.*, vol. 36, no. 2, pp. 246–257, 1997.

[63] V. Pishchik, L. A. Lytvynov, and E. R. Dobrovinskaya, *Sapphire*. 2009.

[64] B. N. J. Persson *et al.*, "Elastic contact mechanics: Percolation of the contact area and fluid squeeze-out," *Eur. Phys. J. E*, vol. 35, no. 1, 2012.

[65] N. Patir and H. S. Cheng, "An Average Flow Model for Determining Effects of Three-Dimensional Roughness on Partial Hydrodynamic Lubrication," *J. Lubr. Technol.*, vol. 100, no. 1, p. 12, 1978.

[66] A. D. Roberts and A. B. Othman, "Rubber Adhesion and the Dwell Time Effect," vol. 42, pp. 119–133, 1977.

[67] S. T. Choi, S. R. Lee, and Y. Y. Earmme, "Measurement of time-dependent adhesion between a polymer film and a flat indenter tip," *J. Phys. D. Appl. Phys.*, vol. 41, no. 7, p. 74023, 2008.

[68] A. Tiwari *et al.*, "The effect of surface roughness and viscoelasticity on rubber adhesion," *Soft Matter*, 2017.

69